

# Cell autonomous regulation of herpes and influenza virus infection by the circadian clock

**Rachel S. Edgar<sup>a</sup>, Alessandra Stangherlin<sup>a</sup>, Andras D. Nagy<sup>a,1</sup>, Michael P. Nicoll<sup>b,2</sup>, Stacey Efstathiou<sup>b,2</sup>, John S. O'Neill<sup>a,3</sup>, Akhilesh B. Reddy<sup>a</sup>**

<sup>a</sup> University of Cambridge Metabolic Research Laboratories, Wellcome Trust-MRC Institute of Metabolic Science, University of Cambridge, Addenbrooke's Hospital, Cambridge CB2 0QQ, UK.

<sup>b</sup> Division of Virology, Department of Pathology, Tennis Court Road, Cambridge, CB2 1QP, UK.

**Correspondence: areddy@cantab.net**

---

<sup>1</sup> Institute affiliation: University of Pecs Medical School, Department of Anatomy, Pecs, Hungary.

<sup>2</sup> Present address: National Institute for Biological Standards and Control, Blanche Lane, South Mimms, Potters Bar, Hertfordshire, EN6 3QG.

<sup>3</sup> Present address: MRC Laboratory of Molecular Biology, Francis Crick Avenue, Cambridge, CB2 0QH, UK.

## **Abstract**

Viruses are intracellular pathogens that hijack host cell machinery and biosynthetic resources to replicate. Rather than being constant, host physiology is rhythmic and undergoes circadian (24 hour) oscillation in a variety of virus-relevant pathways. Whether these daily rhythms impact on viral replication is not known. Here we show that the time of day at which the host is infected regulates virus progression in live mice and in individual cells. Furthermore, we demonstrate that herpes and influenza A virus infections are enhanced when host circadian rhythms are abolished by disrupting the key clock gene *Bmal1*. Intracellular trafficking, biosynthetic processes, protein synthesis and chromatin assembly all contribute to circadian regulation of virus infection. Moreover, herpesviruses differentially target components of the molecular circadian clockwork. Our work thus demonstrates that viruses exploit the clockwork for their own gain, and that the clock therefore represents a novel target for modulating viral replication that extends beyond a single family of these important pathogens.

## **Significance**

The circadian clock coordinates our physiology. Circadian disruption, as occurs during shift work, increases the risk of chronic diseases. For infectious diseases, circadian regulation of systemic immunity is thought to underpin ‘time-of-day’ differences in the response to extracellular pathogens. However, circadian rhythms are cell-autonomous and their interaction with intracellular pathogens, such as viruses, has not been investigated. We demonstrate that the time of day when virus infection occurs has a major impact on disease progression not only in animals but also using cellular models, highlighting that the cellular circadian clock plays a key role in this phenomenon. Disruption of the clock leads to increased virus replication and dissemination, indicating that severity of acute infections can be influenced by circadian timekeeping.

/body

## **Introduction**

Diverse behavioral, physiological and cellular processes exhibit daily (circadian) rhythms, which persist in the absence of external timing cues (1). Cell-autonomous biological clocks drive circadian rhythms observed at the whole organism level, enabling adaptation to the 24-hour solar cycle produced by the Earth's rotation (2). At the molecular level, circadian oscillations are thought to be generated by genetic feedback loops involving the activating transcription factors BMAL1 (ARNTL; Mop3), NPAS and CLOCK. These drive transcription of repressor proteins CRYPTOCHROME1/2 (CRY1/2) and PERIOD1/2 (PER1/2) that feedback to repress their own transcription, with post-translational processes and metabolic activity making an additional contribution to host timekeeping (3-5).

Circadian clocks confer competitive advantage to organisms and their disruption incurs fitness costs. They influence many aspects of human health and disease including sleep/wake cycles and immune function (6-8). Indeed, numerous components of the innate and adaptive immune response are regulated by the circadian clock. The immune response undergoes regeneration and repair as the host transitions to the resting phase of its daily cycle, whereas it is primed for pathogen attack at the onset of the active phase (6, 7). Although changes in host responses to bacterial endotoxin or infection at different times of day have been reported (9, 10), the influence of host circadian clocks on the progression of viral disease is not known. Here, we demonstrate dynamic host-virus interactions over the 24 h day, and show that disrupting the circadian clockwork genetically augments virus replication in mice and cell models.

## **Results**

### **Time of day influences virus infection**

Since viruses are obligate intracellular pathogens, they require a host organism in order to proliferate. Over the course of a day, viruses may encounter host environments that are more or less conducive to replication and dissemination (6, 11-13). We therefore hypothesized that the time of day when infection occurs would influence viral replication. To test this, we infected wild type (WT) mice intranasally with a recombinant *luciferase*-expressing virus, Murid Herpesvirus 4 (*M3:luc* MuHV-4), at two times of day (Fig. 1A; Fig. S1A). As a rodent

pathogen, this virus elicits natural host immune responses and implements evasion strategies in laboratory mice (14, 15), which allow it to establish a latent (or quiescent) infection after primary infection. When WT mice were infected at the onset of their resting phase (Zeitgeber Time 0 (ZT0); “lights on”), virus replication in the nose was 10-fold higher than in mice infected just before they entered their active phase at ZT10 (Fig. 1A). This was under clock control because when we infected *Bmal1*<sup>-/-</sup> mice, which have no overt circadian rhythms (3) (Fig. 1B; Fig. S1B), no difference was seen between groups infected at different times. Furthermore, *Bmal1*<sup>-/-</sup> mice exhibited high levels of MuHV-4 infection when inoculated at either time of day (Fig. S1C-F). Together, these results indicate that the timing of infection in relation the circadian cycle has a major impact on herpesvirus pathogenesis.

### Virus infection is enhanced in *Bmal1*<sup>-/-</sup> mice

Given that infection of *Bmal1*<sup>-/-</sup> mice resulted in high levels of virus replication *in vivo* (Fig. S1D and F), we hypothesized that its role in clock function was important in regulating virus propagation. We therefore longitudinally tracked *M3:luc* MuHV-4 infection in WT and *Bmal1*<sup>-/-</sup> mice, introducing infection into the nose at ZT7 – the time at which BMAL1 is maximally active at genomic sites in peripheral tissues (11),(16, 17). Strikingly, virus replication increased > 3-fold at days 5-7 in *Bmal1*<sup>-/-</sup> mice compared to WT mice (Fig. 2A and B; Fig. S2A). We saw a similar pattern when the acute infection spread to the superficial cervical lymph nodes (SCLN) (Fig. 2A and B). By contrast, latent infection was established to a similar extent in WT and *Bmal1*<sup>-/-</sup> mice (Fig. S2B and C).

To exclude the possibility that elevated infection levels were specific to MuHV-4, we infected mice with a different herpesvirus, Herpes Simplex Virus 1 (HSV-1), by scarification of the left ear. We again tracked the progression and extent of HSV-1 infection using a recombinant virus that encoded *luciferase*, this time under the control of the cytomegalovirus immediate early gene promoter (*CMV:luc* HSV-1) (18). Acute HSV-1 infection was significantly enhanced in arrhythmic *Bmal1*<sup>-/-</sup> mice (Fig. 2C and D; Fig. S2D and E), as seen with MuHV-4. As infection progressed, *Bmal1*<sup>-/-</sup> mice failed to contain HSV-1 spread, which disseminated across the head to the right ear (Fig. 2C and D). Analogous to MuHV-4, although acute infection was more severe when circadian rhythms were disrupted, latent infection was established to a similar extent in both genotypes; an apparent trend towards higher numbers of latent viral genomes in *Bmal1*<sup>-/-</sup> mice was noted, although this did not

reach statistical significance (Fig. S2F), suggesting that the circadian clock principally modulates primary infection *in vivo*.

### Clock-regulated virus replication in cells

A more vigorous immune response to incoming virus at the onset of the active (dark) period could contribute to less MuHV-4 infection at ZT10 *in vivo*. We therefore investigated virus replication at different circadian times in synchronized cell models, which display robust 24 h oscillations but are not subject to systemic immune regulation (Fig. 3A). In order to study the effect of the cellular clock, we used confluent monolayers in which there were limited numbers of dividing cells, and no detectable circadian oscillation in cell cycle activity post-synchronization (Fig. S3; Movie S1). We employed real-time bioluminescence recording systems to monitor both *M3:luc* MuHV-4 replication kinetics with high temporal resolution, and the amount of virus replication as total bioluminescence, which correlated with infectious particle production (Fig. 3B; Fig. S4A-C). Strikingly, when cell populations were infected with MuHV4 at different times *in vitro*, the time-of-day effect on infection observed in mice was recapitulated (Fig. 3C and D): Total bioluminescence is significantly increased in cells infected during the rising phase of *Bmal1* expression (CT18–24, indicated by open arrowheads) compared to cells infected during decline of *Bmal1* expression (CT30–36, indicated by solid arrowheads)(Fig. 3C). Furthermore, infection of cells with MuHV-4 at different times significantly altered the rate of virus replication (Fig. 3D). The entire kinetic profile of infection depended on the circadian phase that the virus encounters, such that slower initial replication rates are associated with prolonged viral gene expression (Fig. 3D; Fig. S4D; Pearson's  $r = 0.999$  (1st cycle) or  $r = 0.982$  (2nd cycle),  $P < 0.01$ ).

Moreover, in agreement with our *in vivo* observations, MuHV-4 infection was significantly increased in primary *Bmal1*<sup>-/-</sup> fibroblasts compared to WT cells (Fig. 4A and B; Movie S2). When synchronized WT and *Bmal1*<sup>-/-</sup> fibroblasts were infected at different circadian times (Fig. S5A; CT of infection indicated by open and solid arrowheads), the time-of-day effect on MuHV-4 infection observed in WT cells was abolished in those from *Bmal1*<sup>-/-</sup> mice (Fig. 4C; Fig. S5B). Additionally, HSV-1 replication is significantly enhanced in *Bmal1*<sup>-/-</sup> cells compared to WT cells (Fig. 4D and E; Movie S3). Thus, the cellular circadian clock exerts a major effect on herpesvirus infection, indicating that our observations in live mice do not simply result from circadian modulation of immune cell function.

Given that cellular circadian rhythms impact on virus replication, we speculated that herpesviruses may manipulate the molecular clockwork during infection. To assess this, we infected mouse NIH3T3 cells expressing luciferase under the control of the *Bmal1* promoter (*Bmal1:luciferase* or *Bmal:luc*) with MuHV-4 at different circadian times (Fig. 5A; Fig. S6A). Interestingly, MuHV-4 acutely induced *Bmal1* expression from ~6 h post-infection, irrespective of the circadian phase at which the cells were infected (one-way ANOVA: peak *Bmal1:luc*,  $P < 0.0001$ ). The subsequent pattern of cellular circadian rhythms during viral infection depended on the time at which cells were infected. Virus-mediated *Bmal1* induction during the endogenous fall in *Bmal1* transcription generated a *Bmal1* peak and disrupted circadian reporter expression (infection at CT18-24, indicated by open arrowhead in Fig. 5A; Fig. S5). In contrast, viral induction at other times (infection at CT30-36; indicated by solid arrowhead in Fig. 5A) enhanced the usual rise in *Bmal1* transcription, and cellular rhythms remained robust for three cycles afterwards (Fig. S6A). These findings strongly suggest that induction of *Bmal1* expression by herpesviruses has different consequences for clock function depending on when in the circadian cycle infection occurs.

Analogous to the arrhythmic *Bmal1*<sup>-/-</sup> *in vivo* and cellular models, enhanced viral replication is observed in cells infected at circadian times when endogenous circadian rhythms are subsequently disrupted (see Fig. 3D and E, and Fig. 5A and B; indicated by open arrowheads). In mouse peripheral tissues that support herpesvirus replication, cellular CT24 corresponds to onset of the rest (light) period (19-21), where rapid, higher levels of replication initially would maximize the chance of transmission during the subsequent active (dark) period 12-24 h later. Cellular CT36 corresponds to the onset of the active period, when slower, lower levels of replication would permit efficient transmission in the following active period 24-36 h later, and perhaps reduce detection at a time when the immune system is primed for pathogen attack.

Critically, expression of repressive clock genes, such as *mCryptochrome1* (*mCry1*) and *mPeriod2* (*mPer2*), was not induced during viral infection (Fig. 5C; Fig. S6B), with a significant, rapid reduction in *mCry1* when cells are infected at CT18 (Fig. 5C). This is consistent with MuHV-4 infection ushering cells from a repressive circadian phase to one where BMAL1 is active, via sustaining *Bmal1* expression and relieving CRYPTOCHROME-mediated repression. Furthermore, HSV-1 infection also acutely upregulated *Bmal1* (Fig. 5D), even more so than MuHV-4, suggesting that *Bmal1* is specifically targeted by both  $\alpha$ - and  $\gamma$ -herpesvirus families. In support of this, *Bmal1* expression is induced in cells

overexpressing viral transcriptional activators from either herpesvirus (Fig. S7), and previous reports have demonstrated an interaction between BMAL1/CLOCK and several HSV-1 transcriptional activators *in vitro* (22, 23).

## Influenza virus infection is augmented in arrhythmic cells

Herpesviruses co-opt cellular transcriptional mechanisms in order to replicate and target clock transcription factors (Fig. 5). We next asked if the impact of BMAL1 ablation on viral infection extended beyond direct transcriptional regulation, to the global changes in cellular physiology that occur when circadian rhythms are disrupted. To investigate this, we infected WT and *Bmal1*<sup>-/-</sup> cells with the orthomyxovirus, influenza A (IAV) (Fig. 6A and B). IAV replicates within the nucleus but encodes its own RNA-dependent RNA polymerase and therefore does not directly employ the host cell's transcriptional machinery for viral gene expression, in contrast to herpesviruses. Remarkably, loss of BMAL1 also significantly augmented IAV protein expression and replication (PB2::GLUC bioluminescence two-way ANOVA: genotype effect,  $P = 0.0004$ ; single-cycle growth two-way ANOVA: genotype effect,  $P = 0.0102$ ). The similar impact of cellular arrhythmicity on two disparate, clinically relevant virus families thus intimates a broader influence of circadian clocks, and specific components such as BMAL1, on viral infection.

## Pathways linking the clock and virus infection

To determine which cellular systems underpin the time-of-day effect on viral replication, we first identified proteins that exhibit a change in abundance between two opposite circadian phases (CT18 vs. CT30) in WT cells. At these times, viral replication in WT, but not in *Bmal1*<sup>-/-</sup> cells, is significantly different (see Fig. 4C). Given that virus infection is augmented in *Bmal1*<sup>-/-</sup> cells at both time points (see Fig. 4C), we then focused on the subset of proteins within this group whose abundance was either increased or decreased at both these times in *Bmal1*<sup>-/-</sup> cells compared with WT cells (Fig. 6C and D; see also Fig. S8). Circadian-regulated proteins expressed at higher levels in *Bmal1*<sup>-/-</sup> cells are enriched for those involved in protein biosynthesis (Figure 6C; see also Figure S8A and Table S1), including amino acid biosynthesis, ribosome structure, translation and protein folding clusters. Additionally,

proteins involved in endoplasmic reticulum function, protein localization and intracellular vesicle trafficking are significantly enriched. This indicates that enhanced capability for viral protein biosynthesis, assembly and egress contribute to clock control of virus replication.

Conversely, circadian-regulated proteins expressed at lower levels in *Bmal1*<sup>-/-</sup> cells are enriched for those involved in organization of the cortical actin cytoskeleton and chromatin assembly (Fig. 6D; see also Figure S8B and Table S2), suggesting that virus particle uncoating, genome trafficking and histone association contribute to clock control of virus replication. Thus, the clock-mediated effects on viral infection in cells can be ascribed to discrete functional categories of protein effectors targeting specific aspects of the virus replication cycle.

## Discussion

Our results show that altering only the time at which the host is infected can significantly alter the extent of virus infection and dissemination *in vivo*, reflecting the profound change in physiology that naturally occurs over the course of a day. Host circadian rhythms underpin this phenomenon, since behaviorally arrhythmic mice do not exhibit time-dependent differences in virus infection. Indeed, the degree to which these intracellular pathogens replicate is a function of circadian time in isolated cells, without systemic circadian cues or host defenses.

For pathogens such as *Plasmodia*, which cause malaria, synchronizing their replication cycle with the host circadian rhythm contributes to their success (24). Likewise, we speculate that co-evolution of viruses with their hosts may have enabled them to capitalize on the predictability of daily rhythms driven by cell-autonomous molecular clocks. Comparable to our findings with herpesviruses, rhythmic gene expression can persist during hepatitis C virus and influenza A virus infection, albeit with altered circadian phase and amplitude (25, 26). Whether such changes to host circadian rhythms enhance virus propagation between cells or transmission between hosts are open questions.

A key feature of cellular clocks is their ability to entrain to external stimuli; initial time-of-day effects would amplify if dysregulated timekeeping cues perpetuate from infected to neighboring uninfected cells. Our results strongly suggest that herpesvirus and IAV replication increases in arrhythmic cells, as demonstrated by virus-induced disruption at

certain circadian times or via loss of BMAL1. However, does this help or hinder persistence at the level of the host or population? HSV-1 disseminates more extensively in *Bmal1*<sup>-/-</sup> mice, for example, but augmented primary productive replication may generate more robust adaptive immune responses.

How do viruses engage with the molecular clockwork and modulate timekeeping? At the simplest level, the circadian activity of host metabolic and trafficking pathways places constraints on replication. In turn, many viruses reprogram cellular metabolism, which can directly feed back to the core clock mechanism. A more intriguing possibility is that viruses can actively gauge the cellular circadian phase via interaction with core clock components, and exploit subsequent circadian variation in replication kinetics. The HSV-1 viral transactivator ICP0 is thought to directly associate with BMAL1, while viral transcription is driven by a complex containing CLOCK (22, 23, 27). But why not associate with CLOCK directly, and why use BMAL/CLOCK at all? The abundance of CLOCK does not oscillate, and its circadian function is bestowed via interaction with BMAL1. We propose that herpesviruses recruit BMAL/CLOCK to tie viral transcription and cellular circadian time.

We found that ICP0 induces *Bmal1* expression outside the context of infection. This implies that *Bmal1* is specifically targeted, rather than a cell-intrinsic innate immune response to infection. However, this presents an apparent paradox, given that replication is enhanced in the absence of BMAL1. Why induce a protein that appears to exert an anti-viral effect? Shifting cells from a repressive circadian phase via concomitant acute induction of *Bmal1* and repression *mCry1* will likely stimulate replication. One straightforward explanation is therefore that chronic arrhythmicity in *Bmal1*<sup>-/-</sup> cells generates a cellular environment less equipped to deal with viral challenge, or that baseline levels of BMAL1 contribute to cell intrinsic anti-viral immune responses (e.g. via interferon signaling). Examining viral pathogenicity in alternate ‘clock knockout’ genetic models, and in hosts subject to chronic circadian desynchrony, will help disentangle such possibilities. This result additionally highlights the complex nature of circadian investigations, in that clock proteins may be co-opted during virus replication in ways unrelated to their timekeeping function (“non-circadian” effects). The global effect of circadian rhythms must be considered, rather than just the effect of individual clock components.

Our work does imply that constitutively low levels of BMAL1 can lead to increased herpes and influenza A viral infection. Remarkably, as well as its daily oscillation, *Bmal1* expression undergoes seasonal variation in human blood samples, with lowest levels during

the winter months (28). We speculate that this could contribute to viral dissemination at the population level since many viruses, including influenza, cause infection more commonly in the winter (29). Interestingly, *Bmal1* controls circadian rhythms in immune cell trafficking and pathogen recognition by induction of Toll-like Receptor 9 (TLR9), highlighting its additional role in adaptive immunity at the whole organism level (30-32). Given that global *Bmal1* expression in macrophages and natural killer cells is substantially lower in mouse models of shift work (chronic jet lag) (33-35), our work suggests that shift workers might be more susceptible to viral disease and would therefore be prime candidates for vaccination against viruses such as influenza. Indeed, timing of influenza vaccine administration in the morning vs. afternoon has recently been shown to be a determinant in systemic immunization response in people aged >65 years (36). Beyond this, acute manipulation of the molecular circadian clockwork may provide a strategy for the development of novel anti-viral therapies.

## Methods

Mice: All animal experimentation was licensed by the Home Office under the Animals (Scientific Procedures) Act 1986, with Local Ethical Review by the University of Cambridge. Animals had *ad libitum* access to regular chow and water, and were maintained at 22°C on a standard 12 h light:12 h dark cycle. Zeitgeber Time (ZT) is defined such that ZT0 is the time of “lights on”, and ZT12 as “lights off” in a standard 12 h light:12 h dark cycle. At the stated ZT, age-matched (6-12 week old) female littermate wild type (WT; *Bmal1*<sup>+/+</sup>) and *Bmal1*<sup>-/-</sup> mice on the C57Bl/6J genetic background were infected intranasally with 1x10<sup>4</sup> plaque forming units (p.f.u.) *M3:luc* MuHV-4 or 5x10<sup>6</sup> p.f.u. *CMV:luc* HSV-1 by scarification of the left ear. Bioluminescence imaging was performed with an IVIS Lumina and signal intensity quantified using Living Image software (Caliper Life Sciences). See SI Methods for further details.

Cell culture and bioluminescence assays: Primary fibroblasts were generated as described previously (37). All cells were propagated in supplemented Dulbecco’s modified Eagle medium (DMEM) containing 4.5 g/l glucose (Sigma D6546), 10% (v/v) FetalClone III serum (Thermo Scientific HyClone), 1X Glutamax (Life Technologies), 100 U penicillin/ml and 100 µg/ml streptomycin (Penicillin–Streptomycin Solution, Sigma P0781). For monitoring of circadian transcriptional rhythms, NIH3T3 fibroblasts (ATCC) were transiently transfected with *mPeriod2:luciferase* (*Per2:luc*), *mCryptochrome1:luciferase* (*Cry1:luc*) or *Bmal1:luciferase* (*Bmal1:luc*) reporter constructs (38). For real-time bioluminescence recordings, confluent cells were temporally synchronized by temperature cycles (32°C:37°C; 12 h:12 h), treatment with 100 nM dexamethasone or serum shock, transferred to “Air Medium” and bioluminescence analyzed using a LumiCycle-32 system (Actimetrics) (39). For comparison between different experiments, and with *in vivo* work, peak *Bmal1:luc* bioluminescence was operationally designated as Circadian Time (CT) = 0/24h. See SI Methods for further details.

Viruses: Wild type (WT) MuHV-4 (MHV-68), M50 MuHV-4 (40), *M3:luciferase* (*M3:luc*) MuHV-4 (15), WT HSV-1 (SC16 strain) and *CMV:luciferase* (*CMV:luc*) HSV-1 (18) stocks were grown in BHK21 cells. Virus titre was determined by plaque assay based on the methodology of Russell (41). PB2::*Gaussia luciferase* (PB2::GLUC) influenza A virus [mouse-adapted strain A/Puerto Rico/8/34 H1N1 (PR8-Gluc)] was a kind gift from Nicholas Heaton and Peter Palese (Icahn School of Medicine at Mount Sinai, New York, USA)(42). WT and PB2::GLUC stocks were amplified (48 h at 37°C) in 10-day old embryonated chicken eggs and stocks titrated by plaque assay. See SI methods for further details

Bioluminescence virus infection assays in cells: For investigation of single-cycle MuHV-4 replication *in vitro*, adherent cells were cultured to confluence, transferred to “Air Medium” (see SI methods) and infected with *M3:luc* MuHV-4 or *CMV:luc* HSV-1 at high multiplicity of infection (MOI = 1-3 p.f.u./cell). Bioluminescence was monitored in real-time using a Lumicycle-32 (Actimetrics), as above, or with a custom Alligator Bioluminescence Incubator

System (Cairn Research, UK). To assess single-cycle influenza A virus (IAV) replication *in vitro*, confluent adherent cells were infected with PB2::GLUC IAV (MOI = 2 pfu/cell). *Gaussia* luciferase is naturally excreted from cells and >60% of total luciferase produced during infection is extracellular (42). Cell culture medium was sampled at the stated times post-infection and luciferase activity subsequently determined using a BioLux *Gaussia* luciferase Assay Kit (NEB E3300L) according to manufacturer's instructions.

**Proteomics:** Synchronized, confluent primary WT and *Bmal1*<sup>-/-</sup> fibroblasts were harvested at either CT = 18h or CT = 30h. Lysates were pre-cleared, reduced with TCEP and alkylated with iodoacetamide. After quenching alkylation with acetone, protein samples were digested with trypsin and labeled with tandem mass tags (TMT) according to the manufacturer's instructions (Thermo). Peptides were dried by vacuum centrifugation and cleaned for LC-MS/MS analysis using C18 Stage Tips with a centrifuge-based protocol. Peptide mixtures were separated on a 50 cm, 75um I.D. Pepmap column over a 3 h gradient at 40°C and eluted directly into the mass spectrometer (Thermo Q Exactive Orbitrap). Xcalibur software was used to control the data acquisition. MaxQuant v1.5.2.8 was used to process the raw data acquired with a reporter ion quantification method. The Uniprot KB database of mouse sequences was used for peptide identification. A peptide estimated false discovery rate (FDR) of 0.1% was used to generate tables with protein and peptide identifications and quantifications. Two-tailed *t*-tests were performed in Perseus using a false discovery rate (FDR) cut-off of 0.05 and a within groups variance  $S_0$  factor of 0.1 (43). Proteins showing significant difference between CT18 and CT30 in WT cells, but not *Bmal1*<sup>-/-</sup> cells, were subsequently tested via two-tailed *t*-test for significant differences between WT and *Bmal1*<sup>-/-</sup> cells at both CT18 and CT30 (FDR cut-off 0.05) and presented graphically in R using the HeatMap package (See Fig. S6C and D). Proteins meeting both significance criteria were then subject to DAVID Functional Annotation Clustering analysis (See Table S1 and Table S2). Outputs were graphically presented using Cytoscape EnrichmentMap application and annotated using Clustermaker Markov Cluster Algorithm and WordCloud (44, 45). See SI Methods for further details.

**Statistical analysis:** Unless otherwise stated, statistical analysis was performed using Prism (GraphPad Software). “*n*” refers to number of biological replicates throughout. For circadian luciferase reporters, moving-average baseline-subtracted (detrended) bioluminescence values were calculated using LumiCycle Data Analysis software (Actimetrics). See SI Methods for further details.

## **Author contributions**

Conceptualization, A.B.R. and R.S.E.; Methodology, A.B.R., R.S.E., J.S.O. and S.E.; Formal Analysis, A.B.R., R.S.E. and J.S.O.; Investigation, R.S.E., A.S., A.D.N, M.P.N., J.S.O and S.E.; Resources, A.B.R., R.S.E. and S.E.; Writing – Original Draft, A.B.R. and R.S.E.; Writing – Review and Editing, A.B.R., R.S.E., J.S.O. and S.E.; Visualization, A.B.R. and R.S.E.; Funding Acquisition, A.B.R.

## **Acknowledgments**

A.B.R. acknowledges funding from the Wellcome Trust (083643/Z/07/Z, 100333/Z/12/Z and 100574/Z/12/Z), the European Research Council (ERC Starting Grant No. 281348, MetaCLOCK), the EMBO Young Investigators Programme, the Lister Institute of Preventative Medicine and the Medical Research Council (MRC\_MC\_UU\_12012/5). A.D.N acknowledges funding from the People Programme (Marie Curie Actions) of the European Union Seventh Framework Programme (FP7/2007-2013; REA grant agreement 627630). We thank L. Ansel-Bollepalli for assistance with animal breeding, I. Robinson for assistance with pilot animal experiments, A. Snijders and H. Flynn (Francis Crick Institute Proteomics Core) for help with proteomics work, Cambridge NIHR BRC Cell Phenotyping Hub for flow cytometry assistance, A. Miyawaki (RIKEN Brain Science Institute, Japan) for Fucci2 lentiviral vectors, and H. Coleman, J. May and M. Jain for helpful discussions. We thank Prof J. Bass (Northwestern University, USA) for *Bmal*<sup>-/-</sup> mouse embryonic fibroblasts used in preliminary experiments, and N. Heaton and P. Palese (Icahn School of Medicine at Mount Sinai, USA) for PB2::*Gaussia* luciferase IAV (PR8 PB2::*GLUC*).

## References

1. Dunlap JC (1999) Molecular bases for circadian clocks. *Cell* 96(2):271-290.
2. Takahashi JS, Hong HK, Ko CH, & McDearmon EL (2008) The genetics of mammalian circadian order and disorder: implications for physiology and disease. *Nature reviews* 9(10):764-775.
3. Bunger MK, *et al.* (2000) Mop3 is an essential component of the master circadian pacemaker in mammals. *Cell* 103(7):1009-1017.
4. van der Horst GT, *et al.* (1999) Mammalian Cry1 and Cry2 are essential for maintenance of circadian rhythms. *Nature* 398(6728):627-630.
5. O'Neill JS, Maywood ES, & Hastings MH (2013) Cellular mechanisms of circadian pacemaking: beyond transcriptional loops. *Handb Exp Pharmacol* (217):67-103.
6. Scheiermann C, Kunisaki Y, & Frenette PS (2013) Circadian control of the immune system. *Nat Rev Immunol* 13(3):190-198.
7. Curtis AM, Bellet MM, Sassone-Corsi P, & O'Neill LA (2014) Circadian clock proteins and immunity. *Immunity* 40(2):178-186.
8. Reddy AB & O'Neill JS (2010) Healthy clocks, healthy body, healthy mind. *Trends in cell biology* 20(1):36-44.
9. Gibbs JE, *et al.* (2012) The nuclear receptor REV-ERB $\alpha$  mediates circadian regulation of innate immunity through selective regulation of inflammatory cytokines. *Proceedings of the National Academy of Sciences of the United States of America* 109(2):582-587.
10. Nguyen KD, *et al.* (2013) Circadian gene Bmal1 regulates diurnal oscillations of Ly6C(hi) inflammatory monocytes. *Science (New York, N.Y)* 341(6153):1483-1488.
11. Koike N, *et al.* (2012) Transcriptional architecture and chromatin landscape of the core circadian clock in mammals. *Science (New York, N.Y)* 338(6105):349-354.
12. Lipton JO, *et al.* (2015) The Circadian Protein BMAL1 Regulates Translation in Response to S6K1-Mediated Phosphorylation. *Cell* 161(5):1138-1151.
13. Bass J & Takahashi JS (2010) Circadian integration of metabolism and energetics. *Science (New York, N.Y)* 330(6009):1349-1354.
14. Stevenson PG & Efstathiou S (2005) Immune mechanisms in murine gammaherpesvirus-68 infection. *Viral immunology* 18(3):445-456.
15. Milho R, *et al.* (2009) In vivo imaging of murid herpesvirus-4 infection. *The Journal of general virology* 90(Pt 1):21-32.
16. Rey G, *et al.* (2011) Genome-wide and phase-specific DNA-binding rhythms of BMAL1 control circadian output functions in mouse liver. *PLoS biology* 9(2):e1000595.
17. Ripperger JA & Schibler U (2006) Rhythmic CLOCK-BMAL1 binding to multiple E-box motifs drives circadian Dbp transcription and chromatin transitions. *Nat Genet* 38(3):369-374.
18. Shivkumar M, *et al.* (2013) Herpes simplex virus 1 targets the murine olfactory neuroepithelium for host entry. *Journal of virology* 87(19):10477-10488.
19. Bando H, *et al.* (2007) Vagal regulation of respiratory clocks in mice. *J Neurosci* 27(16):4359-4365.
20. Zhang R, Lahens NF, Ballance HI, Hughes ME, & Hogenesch JB (2014) A circadian gene expression atlas in mammals: implications for biology and medicine. *Proceedings of the National Academy of Sciences of the United States of America* 111(45):16219-16224.
21. Tanioka M, *et al.* (2009) Molecular clocks in mouse skin. *J Invest Dermatol* 129(5):1225-1231.

22. Kawaguchi Y, *et al.* (2001) Herpes simplex virus 1 alpha regulatory protein ICP0 functionally interacts with cellular transcription factor BMAL1. *Proceedings of the National Academy of Sciences of the United States of America* 98(4):1877-1882.
23. Kalamvoki M & Roizman B (2011) The histone acetyltransferase CLOCK is an essential component of the herpes simplex virus 1 transcriptome that includes TFIID, ICP4, ICP27, and ICP22. *Journal of virology* 85(18):9472-9477.
24. O'Donnell AJ, Schneider P, McWatters HG, & Reece SE (2011) Fitness costs of disrupting circadian rhythms in malaria parasites. *Proceedings. Biological sciences / The Royal Society* 278(1717):2429-2436.
25. Benegiamo G, *et al.* (2013) Mutual antagonism between circadian protein period 2 and hepatitis C virus replication in hepatocytes. *PLoS One* 8(4):e60527.
26. Sundar IK, *et al.* (2015) Influenza A virus-dependent remodeling of pulmonary clock function in a mouse model of COPD. *Sci Rep* 4:9927.
27. Kalamvoki M & Roizman B (2010) Circadian CLOCK histone acetyl transferase localizes at ND10 nuclear bodies and enables herpes simplex virus gene expression. *Proceedings of the National Academy of Sciences of the United States of America* 107(41):17721-17726.
28. Dowell SF (2001) Seasonal variation in host susceptibility and cycles of certain infectious diseases. *Emerg Infect Dis* 7(3):369-374.
29. Dopico XC, *et al.* (2015) Widespread seasonal gene expression reveals annual differences in human immunity and physiology. *Nat Commun* 6:7000.
30. Bussey KA, *et al.* (2014) The gammaherpesviruses Kaposi's sarcoma-associated herpesvirus and murine gammaherpesvirus 68 modulate the Toll-like receptor-induced proinflammatory cytokine response. *Journal of virology* 88(16):9245-9259.
31. Krug A, *et al.* (2004) Herpes simplex virus type 1 activates murine natural interferon-producing cells through toll-like receptor 9. *Blood* 103(4):1433-1437.
32. Silver AC, Arjona A, Walker WE, & Fikrig E (2012) The circadian clock controls toll-like receptor 9-mediated innate and adaptive immunity. *Immunity* 36(2):251-261.
33. Castanon-Cervantes O, *et al.* (2010) Dysregulation of inflammatory responses by chronic circadian disruption. *J Immunol* 185(10):5796-5805.
34. Filipski E, *et al.* (2005) Effects of light and food schedules on liver and tumor molecular clocks in mice. *J Natl Cancer Inst* 97(7):507-517.
35. Logan RW, *et al.* (2012) Chronic shift-lag alters the circadian clock of NK cells and promotes lung cancer growth in rats. *J Immunol* 188(6):2583-2591.
36. Long JE, *et al.* (2016) Morning vaccination enhances antibody response over afternoon vaccination: A cluster-randomised trial. *Vaccine* 34(24):2679-2685.
37. Seluanov A, Vaidya A, & Gorbunova V (2010) Establishing primary adult fibroblast cultures from rodents. *J Vis Exp* (44).
38. Valekunja UK, *et al.* (2013) Histone methyltransferase MLL3 contributes to genome-scale circadian transcription. *Proceedings of the National Academy of Sciences of the United States of America* 110(4):1554-1559.
39. Nagoshi E, *et al.* (2004) Circadian gene expression in individual fibroblasts: cell-autonomous and self-sustained oscillators pass time to daughter cells. *Cell* 119(5):693-705.
40. May JS, Coleman HM, Smillie B, Efstathiou S, & Stevenson PG (2004) Forced lytic replication impairs host colonization by a latency-deficient mutant of murine gammaherpesvirus-68. *The Journal of general virology* 85(Pt 1):137-146.
41. Russell WC (1962) A sensitive and precise plaque assay for herpes virus. *Nature* 195:1028-1029.

42. Heaton NS, *et al.* (2013) In vivo bioluminescent imaging of influenza a virus infection and characterization of novel cross-protective monoclonal antibodies. *Journal of virology* 87(15):8272-8281.
43. Tusher VG, Tibshirani R, & Chu G (2001) Significance analysis of microarrays applied to the ionizing radiation response. *Proceedings of the National Academy of Sciences of the United States of America* 98(9):5116-5121.
44. Merico D, Isserlin R, Stueker O, Emili A, & Bader GD (2010) Enrichment map: a network-based method for gene-set enrichment visualization and interpretation. *PLoS One* 5(11):e13984.
45. Lopes CT, *et al.* (2010) Cytoscape Web: an interactive web-based network browser. *Bioinformatics* 26(18):2347-2348.
46. Proenca JT, Coleman HM, Connor V, Winton DJ, & Efstathiou S (2008) A historical analysis of herpes simplex virus promoter activation in vivo reveals distinct populations of latently infected neurones. *The Journal of general virology* 89(Pt 12):2965-2974.
47. Sakaue-Sawano A, *et al.* (2008) Visualizing spatiotemporal dynamics of multicellular cell-cycle progression. *Cell* 132(3):487-498.
48. Coleman HM, *et al.* (2008) Histone modifications associated with herpes simplex virus type 1 genomes during quiescence and following ICP0-mediated de-repression. *The Journal of general virology* 89(Pt 1):68-77.

## Figure legends

### Fig. 1. Herpesvirus infection in mice is regulated by the circadian clock.

(A) Wild type (WT) female mice were infected with *M3:luciferase* Murid Herpesvirus 4 (*M3:luc* MuHV-4) at either Zeitgeber Time 0 (ZT0) (“lights on”; n=6) or at ZT10 (n=6). The schematic illustrates the anticipated levels of *Bmal1* mRNA and active (genome-bound) BMAL1 protein over the day and night. Extent of infection was monitored by bioluminescence imaging on the days shown. Primary infection in the nose is higher when infection occurs at the onset of the resting period (ZT0) compared with infection just before to the active period (ZT10) (mean±SEM; two-way ANOVA (time of initial infection x time post-infection): time of initial infection effect  $P=0.0021$ ; post-hoc *t*-tests  $*P<0.05$ ). See also Fig. S1A.

(B) Female *Bmal1*<sup>-/-</sup> mice were infected with *M3:luc* MuHV-4 at either ZT0 (n=5) or ZT10 (n=6) and extent of infection was monitored as above (mean±SEM; two-way ANOVA (time of initial infection x time post-infection): time of initial infection effect  $P>0.05$ ; NS = not significant). See also Fig. S1B.

**Fig. 2. Herpesvirus infection is augmented in arrhythmic *Bmal1*<sup>-/-</sup> mice.**

(A) WT (n=6) and *Bmal1*<sup>-/-</sup> (n=5) female mice were intranasally infected with *M3:luc* MuHV-4 at ZT7. Extent and spread of infection was monitored by bioluminescence imaging on the stated days. Representative images (of at least n=5 biological replicates per group) are shown with overlaid bioluminescence radiance measurements.

(B) *M3:luc* MuHV-4 progressively disseminates from the nose to the superficial cervical lymph nodes (SCLN) and is significantly higher in *Bmal1*<sup>-/-</sup> mice (mean±SEM; Nose two-way ANOVA (genotype x time post-infection): genotype effect \**P*=0.0031; Superficial cervical lymph nodes (SCLN) two-way ANOVA (genotype x time post-infection): genotype effect *P*=0.0348; post-hoc *t*-tests \**P*<0.05, \*\**P*<0.01, \*\*\**P*<0.001). For individual data points see Fig. S2A.

(C) Male WT (n=5) and *Bmal1*<sup>-/-</sup> (n=6) mice were infected with *CMV:luciferase* (*CMV:luc*) herpes simplex virus 1 (HSV-1) by scarification of the left ear at ZT7. Extent and spread of infection was monitored by bioluminescence imaging on stated days, as in (A).

(D) *CMV:luc* HSV-1 progressively disseminates from the left ear to the head and right ear, and is increased significantly in *Bmal1*<sup>-/-</sup> mice (mean±SEM; left ear two-way ANOVA (genotype x time post-infection): genotype effect *P*=0.0004; right ear two-way ANOVA (genotype x time post-infection): genotype effect *P*=0.0054; post-hoc *t*-tests \**P*<0.05, \*\**P*<0.01). For individual data points see Fig. S2E.

### Fig. 3. Circadian rhythms modulate herpesvirus replication in cells.

(A) Bioluminescence traces from control (uninfected) temperature-synchronized *Bmall:luciferase* (*Bmall:luc*) and *Per2:luciferase* (*Per2:luc*) circadian reporter NIH3T3 cells (mean±SEM; n=3). Peak *Bmall:luc* bioluminescence is designated Circadian Time 24 (CT24). Colored arrows indicate circadian times (CT) at which parallel cultures of temperature-synchronized NIH3T3 cells were infected with *M3:luc* MuHV-4.

(B) Schematic showing a representative bioluminescence recording and kinetic analysis of *M3:luc* MuHV-4 replication parameters using asymmetrical sigmoidal non-linear regression. See Fig. S4A and B for raw bioluminescence recordings obtained from cells infected at different CTs and  $R^2$  regression coefficients.

(C) Amount of MuHV-4 replication varies significantly depending on the circadian time of infection (mean±SEM; n=3; one-way ANOVA: total bioluminescence  $P=0.0178$ ; multiple comparisons  $*P<0.05$ ). Total bioluminescence calculated by the area under curve method (AUC) and normalized (0% = baseline total bioluminescence between 0 – 1h post-infection, 100% = maximum total bioluminescence values). The variation in total bioluminescence across different CTs is presented (% total bioluminescence – mean % total bioluminescence values for all experimental CTs). See Fig. S4C for Pearson's correlation analysis of total bioluminescence and infectious particle production ( $\text{Log}_{10}$  [plaque-forming units]). Open arrowheads highlight CT18/24 (high infection) and solid arrowheads highlight CT30/36 (low infection).

(D) The rate of viral gene expression varies significantly depending on the circadian time of infection (one-way ANOVA: Hill Slope  $P<0.0001$ ; post-hoc multiple comparisons:  $**P<0.01$ ,  $***P<0.001$ ).

**Fig. 4. Herpesvirus replication is enhanced in *Bmal1*<sup>-/-</sup> cells.**

(A) Pseudo-colored bioluminescence image of wild type (WT) and *Bmal1*<sup>-/-</sup> primary cells infected with *M3:luc* MuHV-4. See also Movie S2.

(B) Representative bioluminescence recordings showing synchronized WT and *Bmal1*<sup>-/-</sup> primary cells infected with *M3:luc* MuHV-4 (mean±SEM; n=3).

(C) Synchronized WT and *Bmal1*<sup>-/-</sup> primary cells were infected with *M3:luc* MuHV-4 at either CT18 or CT30. MuHV-4 replication is significantly increased in *Bmal1*<sup>-/-</sup> cells compared with WT cells (mean±SEM; n=3)(Total bioluminescence (AUC) normalized as for Fig. 3C; two-way ANOVA (genotype x circadian time of infection): genotype effect  $P<0.0001$ ). Time-of-day effect on viral replication is observed in WT cells, but not *Bmal1*<sup>-/-</sup> cells (Total bioluminescence two-way ANOVA (genotype x circadian time of infection): post-hoc multiple comparisons: NS=not significant,  $*P<0.05$ ). See Fig. S4C for correlation analysis of total bioluminescence and infectious particle production ( $\text{Log}_{10}$  [p.f.u.]) and Fig. S5 for circadian reporter controls and *M3:luc* MuHV-4 kinetic analysis.

(D) Pseudo-colored bioluminescence image of wild type (WT) and *Bmal1*<sup>-/-</sup> primary cells infected with *CMV:luc* HSV-1. See also Movie S3.

(E) *CMV:luc* HSV-1 replication is increased significantly in *Bmal1*<sup>-/-</sup> cells compared to WT cells (mean±SEM; n=3). Total bioluminescence (AUC) normalized as for Fig. 3C (two-tailed *t*-test:  $***P<0.001$ ). See Fig. S4E for correlation analysis of total bioluminescence and infectious particle production ( $\text{Log}_{10}$  [p.f.u.]).

**Fig. 5. Virus infection differentially affects clock gene expression.**

(A) Bioluminescence recordings from synchronized *Bmall:luciferase* (*Bmall:luc*) circadian reporter NIH3T3 cells either mock infected or infected with MuHV-4 at CT18 (open arrowhead) and CT30 (solid arrowhead). Mean baseline-subtracted (detrended) bioluminescence (n=3 per group) shown. Infection at CT18 generates an additional peak in *Bmall:luc* expression, disrupting the circadian rhythm, whereas increased *Bmall:luc* expression after infection at CT30 synergizes with circadian *Bmall:luc* expression and rhythms are preserved during infection.

(B) Peak bioluminescence from synchronized *Bmall:luc* cells either mock-infected or infected with MuHV-4 at 3 h intervals from CT18 to CT39 (mean±SEM; n=3). *Bmall:luc* expression is significantly increased, irrespective of the circadian time of infection (one-way ANOVA  $P<0.0001$ ; post-hoc multiple comparisons: \* $P<0.05$ , \*\* $P<0.01$ , \*\*\* $P<0.001$ ). For raw bioluminescence recordings and error boundaries see Fig. S6.

(C) Bioluminescence traces from synchronized *mCryptochrome1:luciferase* (*Cry1:luc*) circadian reporter NIH3T3 cells (mean; n=3). Insert panel shows raw bioluminescence traces (mean±SEM; n=3). *Cry1:luc* is significantly decreased during MuHV-4 infection (post-infection peak bioluminescence two-tailed  $t$ -test \* $P=0.0188$ ).

(D) Bioluminescence recording from synchronized *Bmall:luc* cells mock-infected or infected with HSV-1 at CT36 (solid arrowhead)(mean±s.e.m; n=3). *Bmall:luc* expression is significantly increased during HSV-1 infection (post-infection peak bioluminescence two-tailed  $t$ -test \*\*\* $P<0.001$ ).

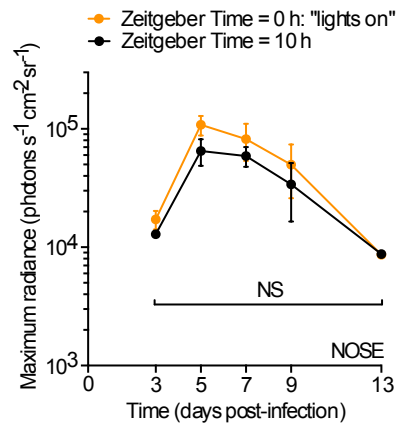
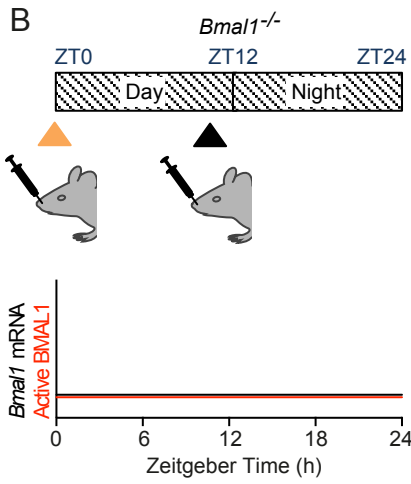
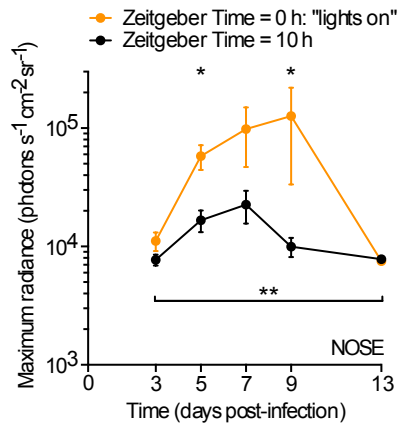
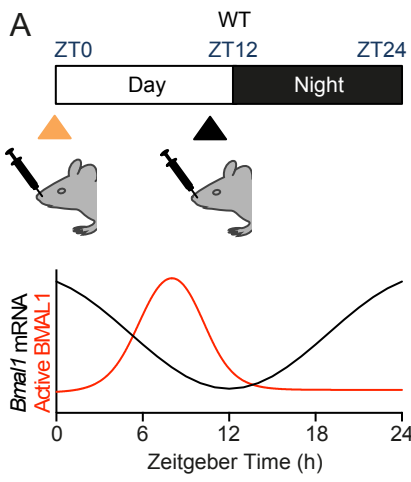
**Fig. 6. Global proteomic comparison of wild type (WT) and *Bmal1*<sup>-/-</sup> cells reveals clock-regulated pathways that impact on viral replication.**

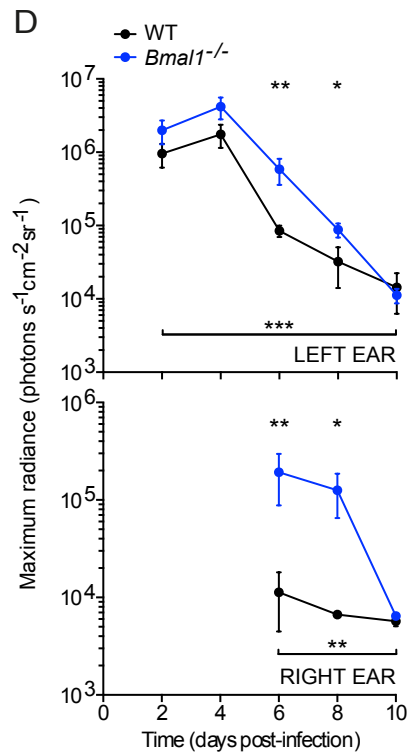
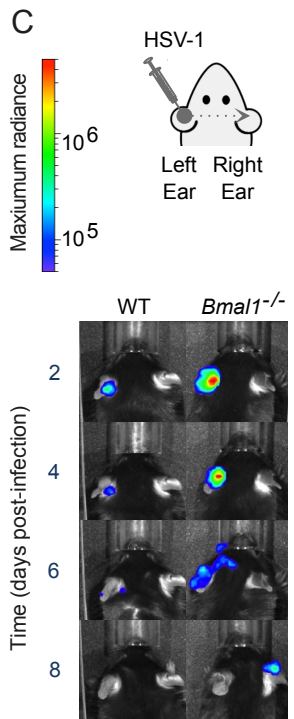
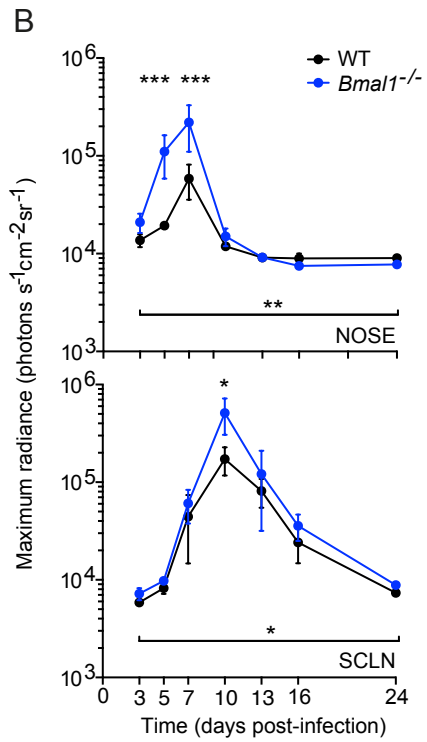
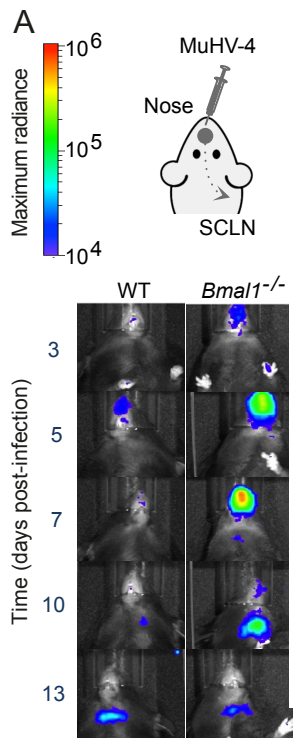
(A) Influenza A viral protein expression is enhanced in *Bmal1*<sup>-/-</sup> cells. WT and *Bmal1*<sup>-/-</sup> cells were infected with PB2::GLUC (*Gaussia luciferase*) influenza A virus (IAV) and emitted photons quantified at stated intervals. PB2 is expressed with more rapid kinetics in *Bmal1*<sup>-/-</sup> compared to WT cells (mean±SEM; n=3; two-way ANOVA (genotype x time post-infection): genotype effect  $P=0.0004$ , interaction  $P<0.0001$ ; post-hoc multiple comparisons:  $*P<0.05$ ,  $**P<0.01$ ,  $***P<0.001$ ). Levels were also higher in *Bmal1*<sup>-/-</sup> cells (sigmoidal non-linear regression: WT  $R^2 = 0.9902$ , *Bmal1*<sup>-/-</sup>  $R^2 = 0.9836$ ; plateau PB2::GLUC bioluminescence two-tailed  $t$ -test:  $***P<0.001$ ;  $F$ -test  $P<0.001$ ; Total PB2::GLUC bioluminescence (AUC) two-tailed Student's  $t$ -test:  $**P<0.0019$ ).

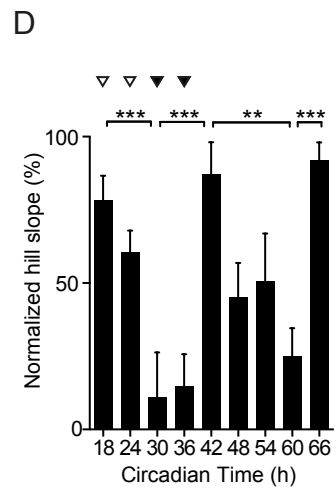
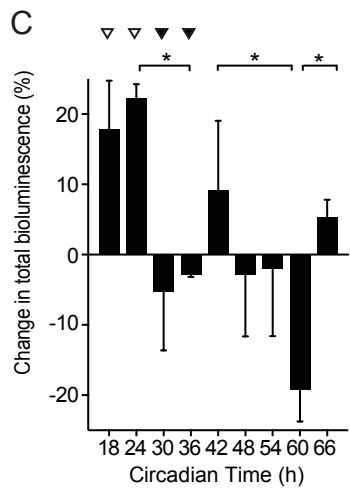
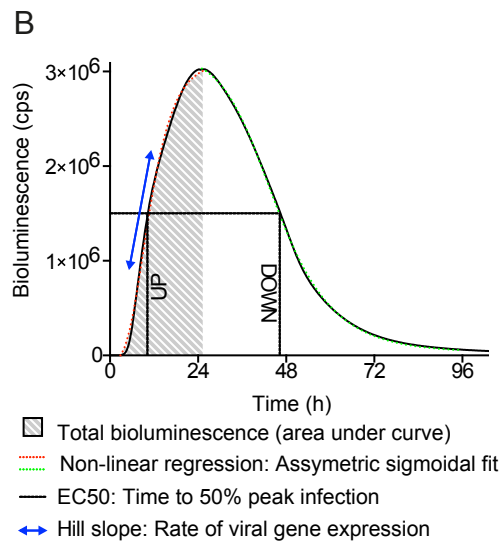
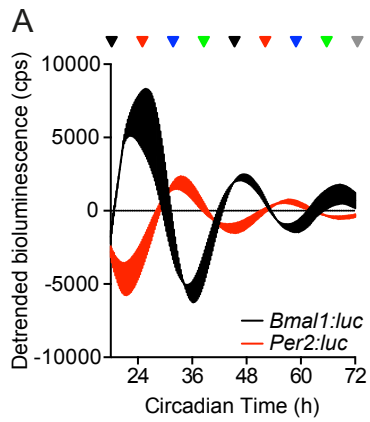
(B) Single-cycle IAV growth is enhanced in *Bmal1*<sup>-/-</sup> cells. At the stated times, IAV-infected cells were harvested and the amount of infectious IAV particles determined by plaque assay. Results shown are representative of two independent experiments. Production of virus particles is significantly enhanced in *Bmal1*<sup>-/-</sup> cells (two-way ANOVA (genotype x time post-infection): genotype effect  $*P=0.0102$ ).

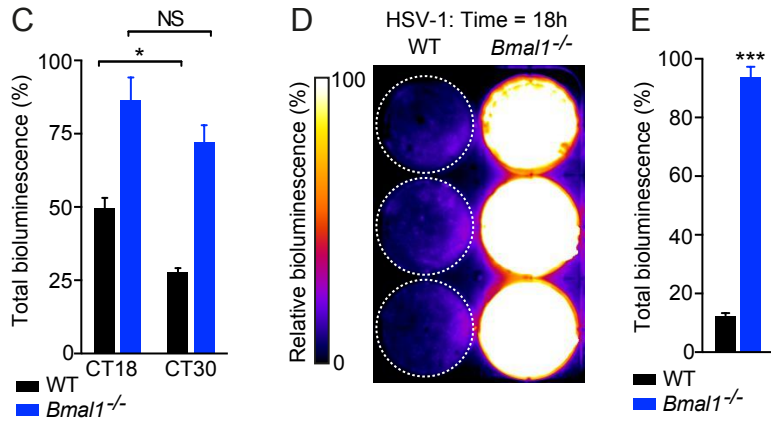
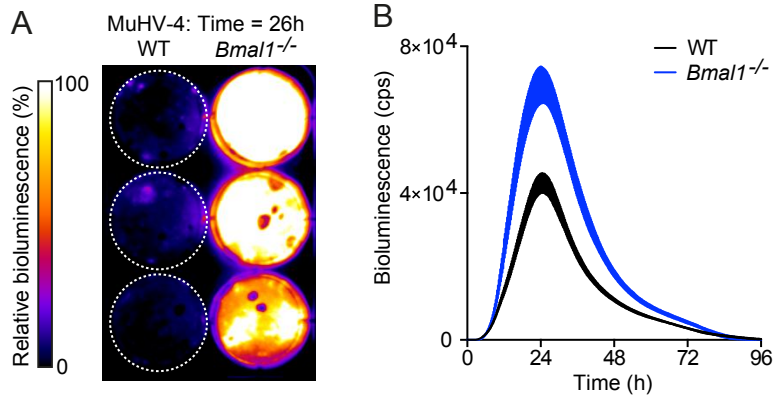
(C) Synchronized WT and *Bmal1*<sup>-/-</sup> primary cells were harvested at CT18 and CT30 and global proteomics performed by liquid chromatography coupled to mass spectrometry. Database for Annotation, Visualization and Integrated Discovery (DAVID) Functional Annotation Clustering analysis was performed on candidate proteins whose abundance significantly changes at CT18 vs. CT30, and is significantly increased in *Bmal1*<sup>-/-</sup> cells compared to WT cells at both CT18 and CT30. Number of proteins is represented by node size and cluster  $P$ -value by node greyscale. Annotations were prescribed by a Markov Cluster Algorithm and text size represents number of nodes per group. A heat map (left) is shown for n=3 biological replicates per genotype and time-point (see also Fig. S8A). Enrichment scores are shown in Table S1.

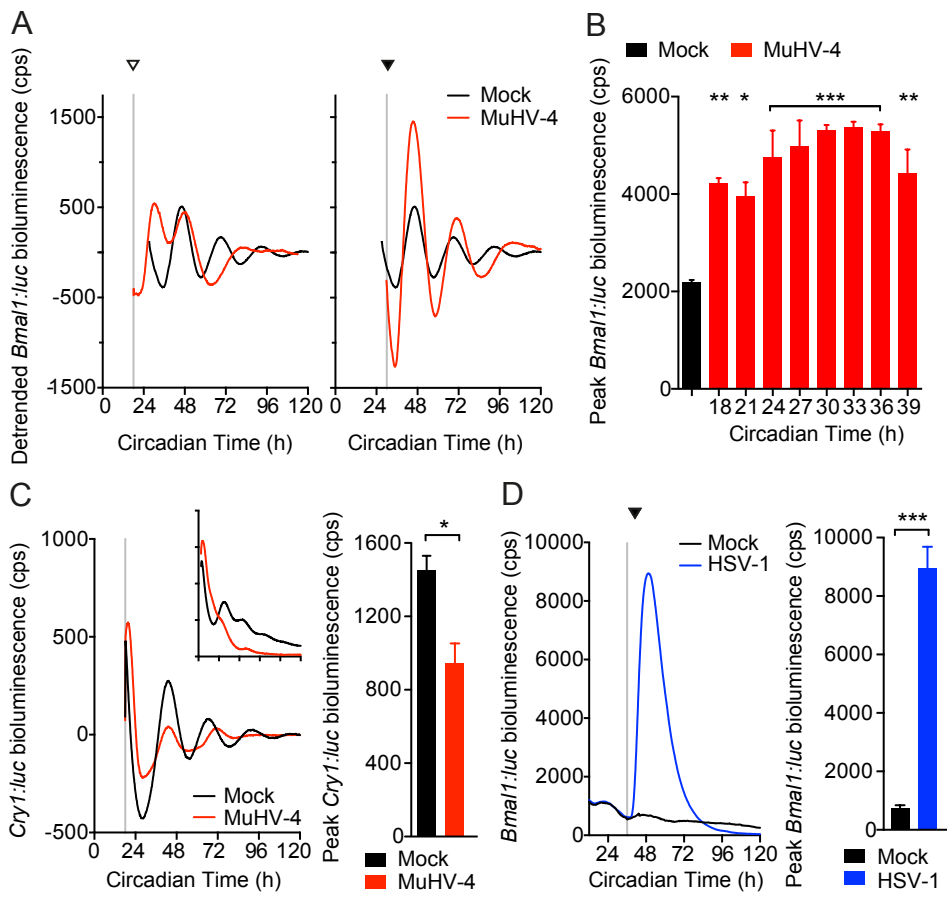
(D) Proteomics analysis performed as in (A). DAVID Functional Annotation Clustering analysis of candidate proteins whose abundance significantly changes at CT18 vs. CT30, and is significantly decreased in *Bmal1*<sup>-/-</sup> cells compared to WT cells at both CT18 and CT30. Proteins are represented as in (A). A heat map (left) is shown for n=3 biological replicates per genotype and time point (see also Fig. S8B). Enrichment scores are shown in Table S2.

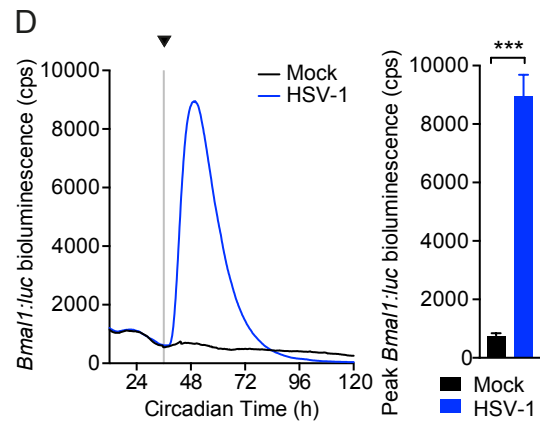
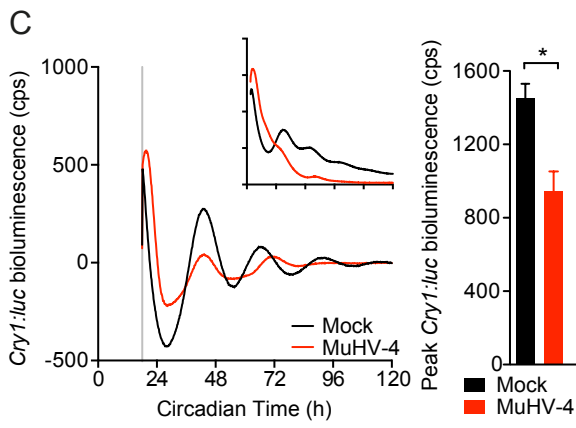
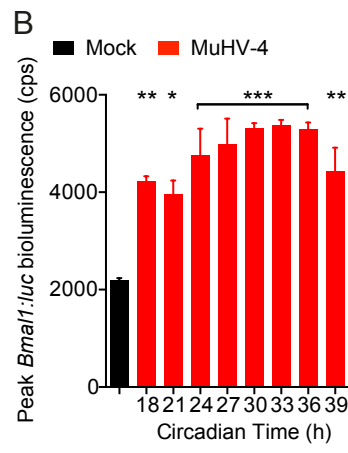
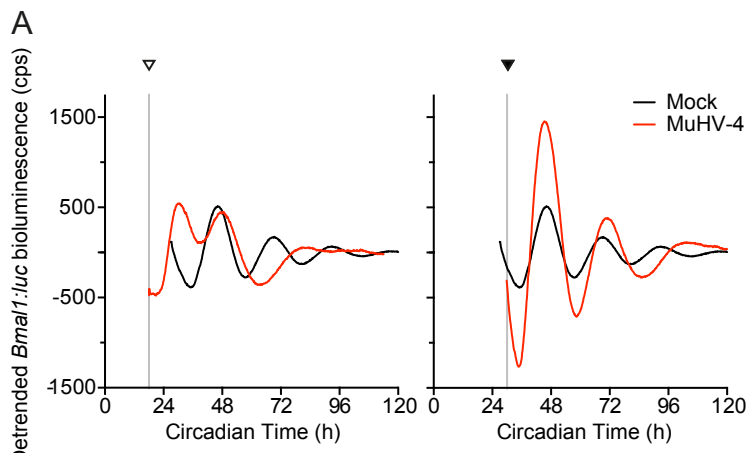


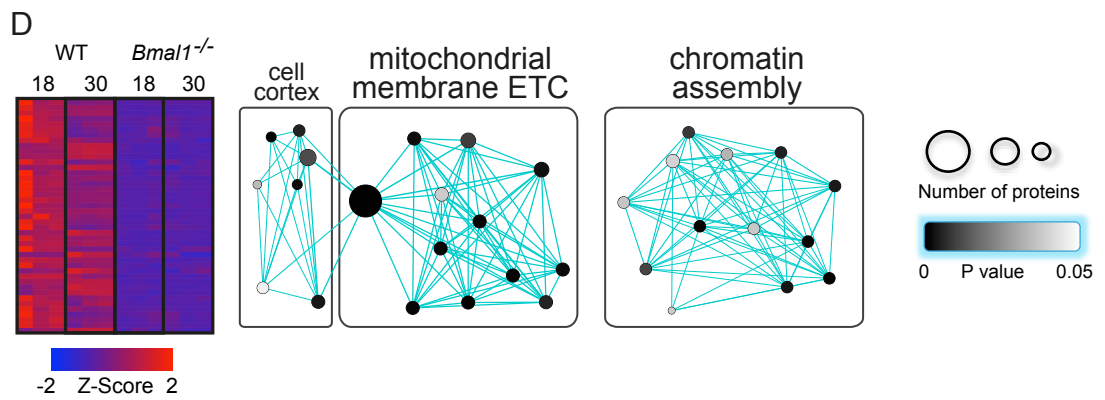
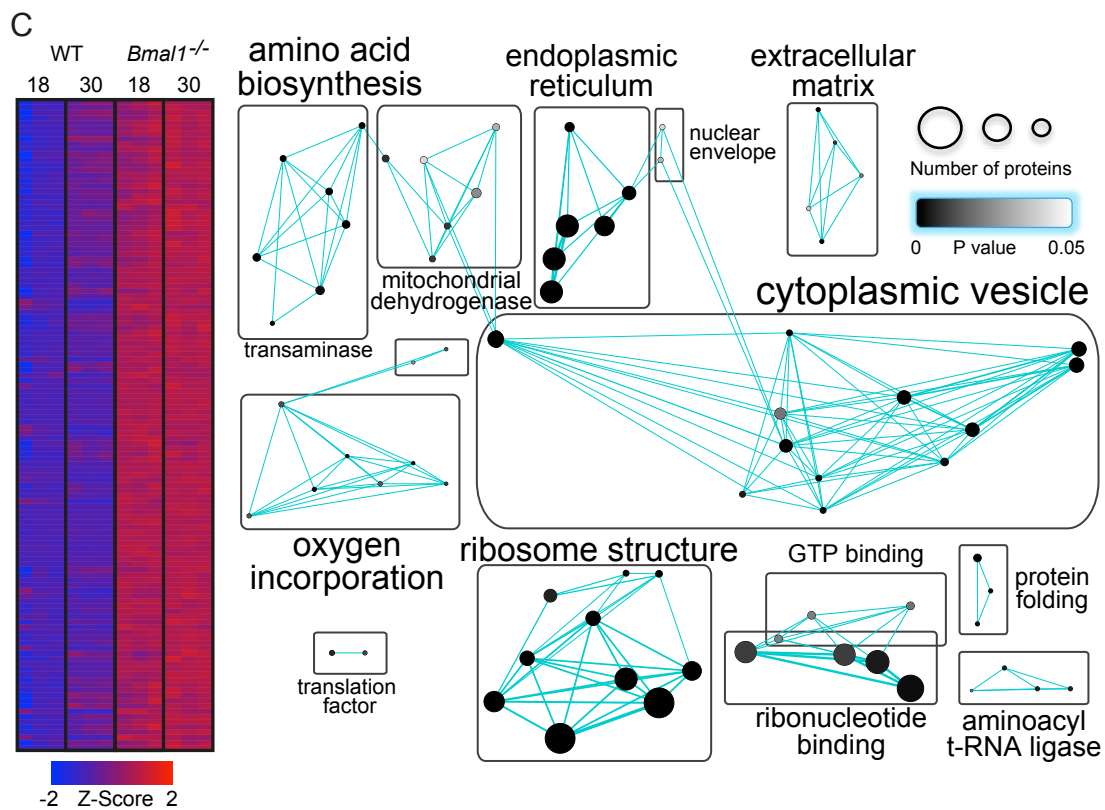
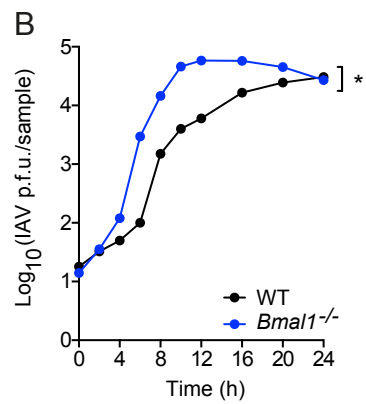
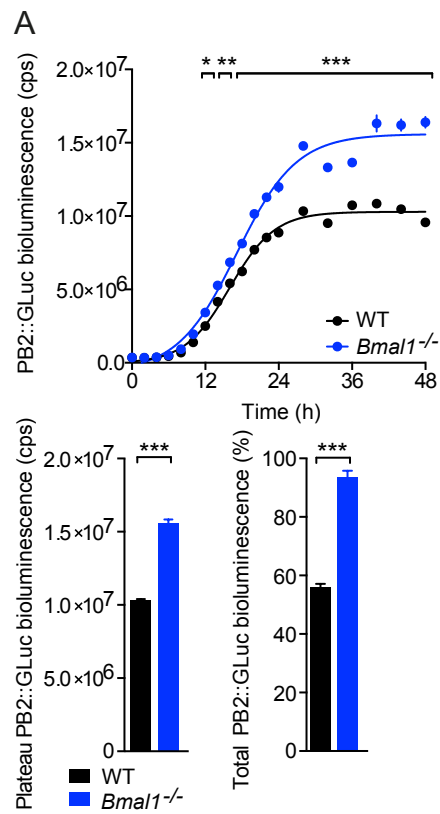












## SI Figure legends

### Fig. S1. *M3:luc* MuHV-4 infection in wild type (WT) and *Bmal1*<sup>-/-</sup> mice infected at ZT0 versus ZT10.

(A) Individual subject plots from Fig. 1A. WT mice show higher levels of MuHV-4 infection at ZT0 vs. ZT10 (mean±SEM; n=6).

(B) Individual subject plots from Fig. 1B. No significant difference in MuHV-4 pathogenesis is observed in *Bmal1*<sup>-/-</sup> mice infected at ZT0 (n=5) and ZT10 (n=6) (mean±s.e.m).

(C) No significant difference in MuHV-4 intranasal infection is observed between WT and *Bmal1*<sup>-/-</sup> mice infected at ZT0 (mean±SEM; n=5 (*Bmal1*<sup>-/-</sup> group), n=6 (WT group)); maximum radiance two-way ANOVA (genotype x time post-infection): genotype effect  $P>0.05$ ; NS=not significant).

(D) MuHV-4 intranasal infection is significantly greater in *Bmal1*<sup>-/-</sup> mice versus WT mice infected at ZT10 (mean±SEM; n=6; maximum radiance two-way ANOVA (genotype x Time post-infection): genotype effect \*\*\* $P<0.001$ ; post-hoc *t*-test \*\* $P<0.01$  \*\*\* $P<0.001$ ).

(E) No significant difference in MuHV-4 infection of the superficial cervical lymph nodes (SCLN) is observed between WT mice infected at ZT0 vs. ZT10, or between *Bmal1*<sup>-/-</sup> mice infected at ZT0 vs. ZT10 (maximum radiance two-way ANOVA (time of infection x time post-infection): time of infection effect  $P>0.05$ , NS=not significant).

(F) MuHV-4 SCLN infection in WT and *Bmal1*<sup>-/-</sup> mice infected at ZT0 and ZT10. SCLN infection is significantly higher in *Bmal1*<sup>-/-</sup> mice vs. WT infected at ZT10 on day 9 post-infection (post-hoc *t*-test \* $P<0.05$ ).

**Fig. S2. *M3:luc* MuHV-4 and *CMV:luc* HSV-1 primary and latent infection in wild type (WT) and *Bmal1*<sup>-/-</sup> mice.**

(A) Individual subject plots from Fig. 2B. During primary infection, MuHV-4 progressively spreads from the nose to SCLN (mean±SEM; n=5 (*Bmal1*<sup>-/-</sup> group), n=6 (WT group)). Infection in the nose and SCLN is significantly higher in *Bmal1*<sup>-/-</sup> mice vs. WT (nose maximum radiance two-way ANOVA (genotype x time post-infection): genotype effect  $P=0.0031$ ; SCLN maximum radiance two-way ANOVA (genotype x time post-infection): genotype effect  $P=0.0348$ ).

(B) 24 days after infection, mice were culled. Latent viral genome loads in the spleen were analysed by quantitative real-time PCR (qPCR), which compares MuHV-4 *M2* gene copy number with cellular *APRT* gene copy number (1000x*M2/APRT*) (mean±SEM; n=5 (*Bmal1*<sup>-/-</sup> group), n=6 (WT group); two-tailed *t*-test  $P>0.05$ ; *F*-test \*\*\* $P=0.0001$ ). See Methods for further details.

(C) Reactivation of latent MuHV-4 in the spleen was assessed by the number infectious centres (plaques) on cell monolayers co-cultured with *ex vivo* splenocytes (mean±SEM; n=5 (*Bmal1*<sup>-/-</sup> group), n=6 (WT group); two-tailed *t*-test  $P>0.05$ ; *F*-test \* $P=0.0228$ ). Thus, no statistically significant difference between mean values of MuHV-4 latent infection was observed by either infectivity assay.

(D) Dissemination of HSV-1 infection from the left ear to the chest is significantly increased in *Bmal1*<sup>-/-</sup> mice vs. WT (chest maximum radiance two-way ANOVA (genotype x time post-infection): genotype effect  $P=0.0037$ ).

(E) Individual subject plots from Fig. 2D. During primary infection, HSV-1 progressively spreads from the left ear to the right ear and chest (mean±SEM; n=5 (WT group); n=6 (*Bmal1*<sup>-/-</sup> group)). Infection in the left ear is significantly higher in *Bmal1*<sup>-/-</sup> mice vs. WT (maximum radiance two-way ANOVA (genotype x time post-infection): genotype effect  $P=0.0004$ ). HSV-1 spreads to secondary sites more effectively in *Bmal1*<sup>-/-</sup> mice vs. WT: n=4 of 6 *Bmal1*<sup>-/-</sup> mice showed substantial infection in the right ear, whereas this is evident in only n=1 of 5 WT mice. Similarly, n=5 of 6 *Bmal1*<sup>-/-</sup> mice showed dissemination of HSV-1 to the chest, versus n=3 of 5 WT mice. Virus infection in the chest is significantly increased in *Bmal1*<sup>-/-</sup> mice compared to WT (maximum radiance two-way ANOVA (genotype x time post-infection): genotype effect  $P=0.0037$ ).

(F) 24 days after infection, mice were culled. Viral genome loads in the dorsal root ganglion were analysed by quantitative real-time PCR (qPCR), which compares HSV-1 *ICP0* gene copy number with cellular *APRT* gene copy number (1000x*ICP0/APRT*). See Methods for further details. No statistically significant difference in HSV-1 latent genome load was observed (two-tailed *t*-test  $P>0.05$ ).

**Fig. S3. Replicative activity of confluent cell monolayers post-synchronization.**

(A) Confluent NIH-3T3 cell monolayers stably transduced with dual FUCCI reporters amCyan::Geminin and mCherry::Cdt1 were trypsinized, stained with DNA dye DRAQ5 and analyzed by flow cytometry. mCherry::Cdt1 is expressed during G1 phase (2n DNA content), whereas amCyan::Geminin is expressed during S/G2 phase ( $2 < n \leq 4$  DNA content).

(B) Representative images of confluent FUCCI reporter NIH-3T3 cell monolayers at different circadian times post-synchronization (red indicates mCherry::Cdt1; blue indicates amCyan::Geminin; see also Movie S1).

(C) Confluent FUCCI reporter NIH-3T3, primary WT and *Bmal1*<sup>-/-</sup> fibroblast monolayers were synchronized and imaged between circadian time (CT) 0 – 66h (see also Movie S1). Cells expressing either amCyan::Geminin or mCherry::Cdt1 were counted at the stated CTs (n = 5 fields of view for each cell type; > 300 cells observed per time point). Across all CTs, G2 phase amCyan::Geminin-positive cells accounted for 5.60±1.4%, 1.70±0.31% and 3.35±0.79% (mean±SEM) of 3T3s, WT and *Bmal1*<sup>-/-</sup> monolayers, respectively. Linear regression analysis shows a significant negative correlation between time post-synchronisation and % G2 phase amCyan::Geminin-positive cells for NIH-3T3 and *Bmal1*<sup>-/-</sup> fibroblasts, but not for WT fibroblasts (3T3s:  $R^2 = 0.9223$ , Pearson  $r = -0.960$ ,  $P < 0.001$ ; *Bmal1*<sup>-/-</sup>:  $R^2 = 0.965$ , Pearson  $r = -0.9780$ ,  $P < 0.001$ ; WT:  $R^2 = 0.317$ , Pearson  $r = -0.563$ ,  $P = 0.1145$ ). Critically, for all three cell types we could detect no circadian oscillation in the ratio of G1 to G2 phase cells. Damped sine wave modeling (non-linear regression) yields best-fit period values > 50h (not within circadian range 18 – 30h) and 2-way ANOVA (cell cycle phase x circadian time): circadian time effect  $P > 0.05$ . Additionally, comparison of cell cycle phase markers between WT and *Bmal1*<sup>-/-</sup> cell types at each circadian time by multiple two-tailed t-tests revealed no significant results (false discovery rate (FDR)  $Q = 1\%$ ).

**Fig. S4. Kinetics and total amount of MuHV-4 single-cycle replication are a function of the circadian time at which cells are infected.**

(A) Raw bioluminescence recordings from temperature-synchronized NIH3T3 cells infected with *M3:luc* MuHV-4 at 6h intervals from CT42-CT66 (mean; n=3). cps = counts per second.

(B) Coefficients of determination ( $R^2$ ) for asymmetric sigmoidal non-linear regression of data from Fig. 3.

(C) Parallel cultures of primary WT fibroblasts were incubated with *M3:luc* MuHV-4 at different multiplicities of infection (MOI) between 0.001 - 2 plaque-forming units (p.f.u.) per cell. After 2h, cells were acid-washed to remove the input virus. Real-time bioluminescence was recorded and the amount of infectious MuHV-4 particles produced at 0, 12, 24, 48 and 96h post-infection was determined by plaque assay (mean $\pm$ SEM; n=3). Over this range of MOI, total bioluminescence during exponential growth (area under curve, AUC) linearly correlates with  $\text{Log}_{10}$  (p.f.u) (linear regression analysis:  $R^2 = 0.677$ ,  $P < 0.0001$ ; Pearson's  $r = 0.823$ ; a 23.56% difference in total bioluminescence  $\approx$  10-fold change p.f.u.).

(D) Time to 50% peak infection and 50% decrease in peak infection varies significantly depending on the circadian time of infection (mean $\pm$ SEM; n=3; one-way ANOVA: time to 50% peak infection  $P=0.0002$ ; one-way ANOVA: time to 50% decrease in peak infection,  $P < 0.0001$ ; post-hoc multiple comparisons:  $**P < 0.01$   $***P < 0.001$ ). Over each circadian cycle, there is a significant linear correlation between the time to 50% peak infection and the time to 50% decrease in peak infection (Pearson's  $r=0.999$  (1st cycle)  $P=0.022$ ; or  $r=0.982$  (2nd cycle)  $P=0.006$ ). Infection is sustained less robustly at circadian times that yield more rapid viral gene expression initially, with the entire kinetic profile of infection depending on the circadian time of infection.

(E) Parallel cultures of NIH-3T3 fibroblasts were incubated with *CMV:luc* HSV-1 at different multiplicities of infection (MOI) between 0.001 - 10 p.f.u. per cell. After 1h, cells were acid-washed to remove the input virus. Real-time bioluminescence was recorded and the amount of infectious MuHV-4 particles produced at 0, 8, 24, 48 and 72h post-infection was determined by plaque assay (mean $\pm$ SEM; n=3). Over this range of MOI, total bioluminescence during exponential growth (AUC) linearly correlates with  $\text{Log}_{10}$  (p.f.u) (linear regression analysis:  $R^2 = 0.706$ ,  $P = 0.0002$ ; Pearson's  $r = 0.840$ ; 15.9% difference in total bioluminescence  $\approx$  10-fold change p.f.u.).

**Fig. S5. Circadian time effect on MuHV-4 kinetics in WT but not *Bmal1*<sup>-/-</sup> cells.**

(A) Dexamethasone-synchronized *mPeriod2:luciferase* (*Per2:luc*) and *Bmal1:luciferase* (*Bmal1:luc*) circadian reporter fibroblasts (mean±SEM; n=3). Circadian controls for synchronization protocol used in Fig. 4C, Fig. 6C and D. In Fig. 4C, dexamethasone-synchronized WT and *Bmal1*<sup>-/-</sup> primary cells were infected with *M3:luc* MuHV-4 at either CT18 (open arrowhead) or CT30 (solid arrowhead).

(B) Kinetic analysis of experiment described in Fig. 4C. Kinetic analysis was performed as shown in Fig. 3B ( $R^2$  regression coefficients: WT CT18 = 0.9782, WT CT30 = 0.9932, *Bmal1*<sup>-/-</sup> CT18 = 0.9668, *Bmal1*<sup>-/-</sup> CT30 = 0.9768). Time to 50% peak infection is significantly decreased in *Bmal1*<sup>-/-</sup> cells compared with WT cells (two-way ANOVA (genotype x circadian time of infection): genotype effect  $P < 0.0001$ ). Time-of-day effect on viral replication is observed in WT cells, but not *Bmal1*<sup>-/-</sup> cells (time to 50% peak infection two-way ANOVA (genotype x circadian time of infection): post-hoc multiple comparisons: NS=not significant, \*\*\* $P < 0.001$ ).

**Fig. S6. MuHV-4 infection rapidly induces *Bmall* expression.**

(A) Raw and detrended (baseline-subtracted) bioluminescence recordings from synchronized *Bmall:luc* circadian reporter NIH3T3 cells either mock-infected or infected with MuHV-4 at 3 h intervals from CT=18h to CT=39h (CT=circadian time). Grey lines indicate CT of infection. Top panel: raw *Bmall:luc* bioluminescence recordings (counts per second, cps) (mean±SEM boundaries; n=3). Bottom panel: detrended *Bmall:luc* bioluminescence analysis (moving-average subtracted; mean±SEM boundaries; n=3). Selected data are presented in Fig. 5A (infection at CT=18 and 30h) and peak *Bmall:luc* bioluminescence data are summarized in Fig 5B.

(B) Bioluminescence traces from synchronized *Per2:luc* circadian reporter NIH3T3 cells (mean; n=3) either mock-infected or infected with MuHV-4 (grey line indicates CT of infection). Insert panel shows raw bioluminescence traces (mean±SEM).

**Fig. S7. *Bmall* expression is induced in cells overexpressing herpesvirus transcriptional activators.**

(A) Synchronized NIH3T3 cells expressing *Bmall:luc* transcriptional reporter were either mock-infected or infected with wild type (WT) MuHV-4 or M50 MHV-68, a recombinant virus that overexpresses ORF50, which encodes the main viral transcriptional transactivator. *Bmall:luc* bioluminescence is significantly increased during M50 MuHV-4 infection, compared with WT MuHV-4 or mock infected controls (mean±SEM; n=3; one-way ANOVA:  $P=0.0049$ ; post-hoc multiple comparisons:  $*P<0.05$ ,  $**P<0.01$ ).

(B) An adenoviral Tet-On system was used to investigate whether the HSV-1 viral transactivator Infected Cell Polypeptide 0 (ICP0) can initiate *Bmall* transcription. Synchronized NIH3T3 cells expressing the *Bmall:luc* transcriptional reporter were infected with adenoviral constructs expressing rtTA from the HCMV IE promoter (Ad.CMV.rtTA), ICP0 under the control of a Tetracycline-Responsive (TRE) promoter (Ad.TRE.ICP0), a non-functional RING-finger deletion mutant (FXE) of ICP0 under the control of a TRE promoter (Ad.TRE.FXE), or a combination thereof. Doxycycline (Dox) was added 46 h after infection to enable transcription from the TRE promoter if rtTA is present. ICP0 significantly increases *Bmall:luc* (% change 3h pre-Dox vs. 3h post-Dox addition) compared to controls (mean±SEM; n=3; one-way ANOVA:  $P=0.0038$ ; post-hoc multiple comparisons:  $**P<0.01$ ,  $***P<0.001$ ).

**Fig. S8. Proteins that show significantly different expression levels at between WT and *Bmal1*<sup>-/-</sup> cells.**

(A) Proteins whose abundance significantly changes at CT18 vs. CT30, and is significantly increased in *Bmal1*<sup>-/-</sup> cells compared to WT cells at both CT18 and CT30. See Fig. 6C and Table S1 for Database for Annotation, Visualization and Integrated Discovery (DAVID) Functional Annotation Clustering analysis.

(B) Proteins whose abundance significantly changes at CT18 vs. CT30, and is significantly decreased in *Bmal1*<sup>-/-</sup> cells compared to WT cells at both CT18h and CT30. See Fig. 6D and Table S2 for DAVID Functional Annotation Clustering analysis.

**Table S1. Enrichment cluster scores and *P*-values of DAVID enrichment analysis.**

DAVID Functional Annotation Clustering analysis for candidate proteins whose abundance significantly changes at CT18 vs. CT30, and is significantly increased in *Bmal1*<sup>-/-</sup> cells compared to WT cells at both CT18 and CT30. Gene ontology terms with *P*<0.05 shown. See Fig. 6C for diagrammatic presentation of results.

**Table S2. Enrichment cluster scores and *P*-values of DAVID enrichment analysis.**

DAVID Functional Annotation Clustering analysis for proteins whose abundance significantly changes at CT18 vs. CT30, and is significantly decreased in *Bmal1*<sup>-/-</sup> cells compared to WT cells at both CT18 and CT30. Gene ontology terms with *P*<0.05 shown. See Fig. 6D for diagrammatic presentation of results.

### **Movie S1. FUCCI cell cycle reporter expression in confluent NIH-3T3 cells**

Confluent FUCCI mCherry::Cdt1(G1 phase)/amCyan::Geminin(S/G2 phase) reporter NIH-3T3 cell monolayers were synchronized and imaged between circadian time (CT) 0 – 66h. Cells expressing the G2 phase marker amCyan::Geminin (blue) account for < 20% of the total number and no circadian rhythm in mCherry::Cdt1/amCyan::Geminin ratio is observed (see also Fig. S3).

### **Movie S2. MuHV-4 replication is enhanced in *Bmall*<sup>-/-</sup> cells**

Pseudo-colored bioluminescence recording of wild type (WT) and *Bmall*<sup>-/-</sup> primary cells infected with *M3:luc* MuHV-4.

### **Movie S3. HSV-1 replication is enhanced in *Bmall*<sup>-/-</sup> cells.**

Pseudo-colored bioluminescence recording of wild type (WT) and *Bmall*<sup>-/-</sup> primary cells infected with *CMV:luc* HSV-1.

## SI Methods

### Mice

Sample size was determined using the resource equation:  $E$  (degrees of freedom in ANOVA) = (total number of experimental animals) – (number of experimental groups), with sample size adhering to the condition  $10 < E < 20$ . For comparison of MuHV-4 and HSV-1 infection in WT versus *Bmall*<sup>-/-</sup> mice at ZT7 (Fig. 2), investigator did not know the genotype of the animals when conducting infections, bioluminescence imaging and quantification. For bioluminescence imaging, mice were injected intraperitoneally with endotoxin-free luciferin (Promega E6552) using 2 mg total per mouse. Following anaesthesia with isoflurane, they were scanned with an IVIS Lumina (Caliper Life Sciences), 15 min after luciferin administration. Signal intensity was quantified using Living Image software (Caliper Life Sciences), obtaining maximum radiance for designated regions of interest (photons per s per cm<sup>2</sup> per Steradian: photons s<sup>-1</sup> cm<sup>-2</sup> sr<sup>-1</sup>), relative to a negative control region. At 24 days post-infection, mice were culled and tissue removed for analysis of latent infection.

### Analysis of virus latency

For analysis of MuHV-4 latent infection in mice, viral genome loads were measured by real-time PCR using DNA extracted from spleen tissue as previously described (15). MuHV-4 *M2* gene were amplified using a Rotor Gene 3000 (Corbett Research) and PCR products quantified by hybridization with a Taqman probe. Genome copy number was determined by comparison to a standard curve of cloned *M2* plasmid templates. Cellular DNA was quantified in parallel by amplifying part of the *adenosine phosphoribosyl transferase* gene (*APRT*) and the ratio of MuHV-4 genome copies to *APRT* determined. Reactivation of latent MuHV-4 was measured by infectious centre assay: Spleens were disrupted into single-cell suspensions and serial dilutions were co-cultured with cell monolayers. After 6 days, cells were fixed and stained for plaque counting, as above. For analysis of HSV-1 latent infection in mice, viral genome loads were measured by real-time PCR using DNA extracted from dorsal root ganglion tissue as previously described (46). HSV-1 *ICP0* gene were amplified using a Rotor Gene 3000 and PCR products quantified by hybridization with a Taqman probe. Genome copy number was determined by comparison to a standard curve of cloned *ICP0* plasmid templates. Cellular DNA was quantified in parallel by amplifying part of the *APRT* gene and the ratio of HSV-1 genome copies to *APRT* determined.

### Cell culture and bioluminescence assays

All cells were propagated in Dulbecco's modified Eagle medium (DMEM) containing 4.5 g/l glucose (Sigma D6546) was supplemented with 10% (v/v) FetalClone III serum (Thermo Scientific HyClone), 1X Glutamax (Life Technologies), 100 U penicillin/ml and 100 µg/ml streptomycin (Penicillin–Streptomycin Solution, Sigma P0781). Transfections were conducted using GeneJuice transfection reagent

(Millipore). After synchronization, cells were transferred to “Air Medium”, containing [DMEM (Sigma D5030) supplemented with 5 g/l glucose, 20 mM HEPES, 100 U penicillin/ml and 100 µg/ml streptomycin, 0.035% NaHCO<sub>3</sub>, FetalClone III serum, 1X Glutamax, 2X B-27® Supplement (Life Technologies 17504-044) and 0.3 mM Luciferin (Biosynth L8220)]. All experiments were initiated > 24 h after cells were transferred to constant conditions, so that they would not be subject to any effects of the synchronization treatment. Bioluminescence was monitored using a LumiCycle-32 system (Actimetrics) and recordings were analysed using LumiCycle Data Analysis software (Actimetrics).

### Cell cycle analysis of confluent cell monolayers

NIH-3T3, primary WT and *Bmal1*<sup>-/-</sup> fibroblasts were sequentially transduced with lentiviral fluorescent ubiquitin-based cell cycle indicators (FUCCI) mCherry::Cdt1 and amCyan::Geminin reporters (47). Dual reporter-positive cells were selected by FACS (Influx Cell Sorter, BD Biosciences) and seeded into 35mm dishes for subsequent analysis. To confirm that expression of mCherry::Cdt1 and amCyan::Geminin correspond to G1 (2n DNA content) and S/G2 (2<n≤4 DNA content) cell cycle phases, respectively, cells were stained with DNA dye DRAQ5 (abcam) and analysed by flow cytometry (LSR-Fortessa, BD Biosciences). To examine dynamics of replicative activity under experimental confluent conditions, synchronized FUCCI reporter monolayers were observed by time-lapse live cell imaging over 3 days (Nikon Eclipse Ti-E inverted epifluorescent microscope). At stated circadian times, numbers of mCherry::Cdt1- and amCyan::Geminin-positive cells were counted and their ratio determined.

### Viruses

To generate MuHV-4 and HSV-1 stocks, infected BHK21 cells were harvested following the development of cytopathic effect. Virus titre was determined by plaque assay as follows. For MuHV-4, BHK21 or NIH 3T3 cell monolayers were incubated (2 h at 37°C) with 10-fold dilutions of virus then overlaid with 0.6% carboxymethylcellulose to limit progeny virus spread to adjacent cells only. After 4 days, cells were fixed in 10% formaldehyde and stained with 0.1% toluidine blue for plaque counting. For HSV-1, BHK21 cells were incubated (45 min at 37°C) in suspension with 10-fold dilutions of virus before supplementation with 1% carboxymethylcellulose. After 1-2 days, cells were fixed in 10% formaldehyde and stained with 0.1% toluidine blue for plaque counting. For IAV titration, Madin Darby canine kidney (MDCK) cell monolayers were incubated (1 h at 37°C) with virus in serum-free medium then overlaid with 1.2% Avicel® (IMCD)/DMEM plus 1µg/ml TPCCK-trypsin (Worthington Biochemical), 0.14% BSA (Sigma) and 1X Glutamax (Life Technologies). After 2 days, cells were fixed in 10% formaldehyde and stained with 0.1% toluidine blue for plaque counting. Additionally, single-cycle growth curves were performed as follows: Parallel cell cultures were infected with WT IAV

(MOI = 5 pfu/cell; 37°C) and after 1 h any remaining input virus was removed by acid washing (40 mM citric acid, pH 3, 135 mM NaCl, 10 mM KCl). At stated times post-infection, cultures were harvested and stored at -80°C. The amount of infectious virus produced within the time stated was determined by plaque assay as above.

### Correlation of viral bioluminescence and infectious particle production

To correlate *M3:luciferase* MuHV-4 (*M3:luc* MuHV-4) and *CMV:luciferase* HSV-1 (*CMV:luc* HSV-1) bioluminescence with production of infectious particles, parallel confluent fibroblast monolayers were incubated with luciferase viruses at a range of multiplicities of infection (MOI; 2 - 0.001 p.f.u./cell for *M3:luc* MuHV-4; 10 – 0.001 p.f.u./cell for *CMV:luc* HSV-1). Input virus was then removed by acid washing (40 mM citric acid, pH 3, 135 mM NaCl, 10 mM KCl). Bioluminescence was monitored in real-time using a Lumicycle-32 (Actimetrics). At stated times post-infection, parallel cultures were harvested and stored at -80°C. The amount of infectious virus produced was determined by plaque assay. The total bioluminescence acquired during stated times post-infection was determined by the area under curve (AUC) method. Correlation analysis was performed using linear regression (Total bioluminescence vs. Log<sub>10</sub> (p.f.u.) produced by equivalent cultures over the same time frame during exponential growth).

### ICP0 *in vitro* expression assay

Infected Cell Polypeptide 0 (ICP0) adenoviral vectors were a kind gift from Anna Salvetti and Marie-Claude Geoffroy (INSERM U649, Nantes, France). This Tet-On system comprises Ad.CMV.rtTA (expressing rtTA from the HCMV immediate early promoter), Ad.TRE.ICP0 (expressing ICP0 from a Tetracycline-Responsive (TRE) promoter) and Ad.TRE.FXE (expressing a non-functional RING-finger deletion mutant (FXE) of ICP0 from a TRE promoter) as previously described (48). NIH3T3 cells expressing the *Bmall:luc* reporter construct were infected with the adenovirus vectors alone or in combination (Ad.CMV.rtTA: MOI = 10 pfu/cell; Ad.TRE.ICP0 or Ad.TRE.FXE: MOI = 4 pfu/cell). After 46 h of bioluminescence recording, doxycycline (Dox) was added (1 µg/ml) and bioluminescence recording resumed.

### Proteomics: Lysis and alkylation

Primary fibroblasts from wild type (WT; *Bmall*<sup>+/+</sup>) and *Bmall*<sup>-/-</sup> mice were grown to confluence in 6-well plates (n=3 per time point) and synchronized with 100 nM dexamethasone for 20 minutes, their medium exchanged, and then incubated under constant conditions (37°C in darkness). Cells were then harvested by briefly washing with ice-cold PBS and incubating with lysis buffer (250 mM HEPES, 1% SDS, 1% NP-40, 10 mM DTPA) for 20 minutes. The first time-point was designated Circadian Time (CT) 18, and the other CT30 based on the assessment of cells expressing the *Bmall:luc* or the *Per2:luc* reporter that were synchronized in parallel (see Fig. 3C and Fig. 4C). After scraping the cell monolayers into 1.5ml tubes, lysates were pre-cleared by centrifugation at 16,100 rpm in a bench top microfuge for 10 minutes at 4°C.

Protein concentration was determined using the BCA Protein Assay Kit (Thermo Pierce) and 100 µg per condition transferred into a new tube. The final volume was adjusted to 100µl with lysis buffer. The samples were then reduced with 5 µl of 200 mM TCEP and incubated at 55°C for 1 h. 5 µl of 375 mM iodoacetamide was added to alkylate proteins and incubated for 30 minutes, protected from light, at room temperature. The alkylation reaction was quenched by adding 600 µl of ice-cold acetone and protein precipitated by incubating at -20°C overnight. On the following day, the samples were centrifuged at 16,100 rpm in a bench top microfuge for 15 minutes at 4°C. Acetone was removed and the pellets air-dried for 5 minutes at room temperature.

### Proteomics: Digestion and tandem mass tag (TMT) labelling

Acetone-precipitated pellets were resuspended in 100 µl of 100mM TEAB aided by sonication on ice for 10 cycles (30 seconds on; 30 seconds off; medium power) in a Bioruptor sonicator. Trypsin (2.5 µg Promega Trypsin Gold) per 100 µg protein sample, and incubated for 1 h at 37°C. After the initial incubation a further 2.5 µg trypsin was added and the digestion allowed to proceed overnight at 37°C. TMT labelling was performed according to the manufacturer's instructions (Thermo). Briefly, the TMT labelling reagents were resuspended by adding 82 µl anhydrous acetonitrile (ACN) to each vial. Then, 41 µl of the TMT reagent was added to the digested proteins and incubated for 1 h at room temperature with occasional vortexing. 8 µl of 5% hydroxylamine was then added to the samples and incubated for 15 minutes at room temperature to quench the reaction. TMT-labelled samples were combined after elution at equimolar ratios (as below) and dried by vacuum centrifugation.

Wild type: CT18 vs. CT30

TMT label	Time point
126	Wild type CT30 Rep A
127	Wild type CT30 Rep B
128	Wild type CT30 Rep C
129	Wild type CT18 Rep A
130	Wild type CT18 Rep B
131	Wild type CT18 Rep C

*Bmal1*<sup>-/-</sup> CT18 vs. CT30

TMT label	Time point
126	<i>Bmal1</i> <sup>-/-</sup> CT18 Rep A
127	<i>Bmal1</i> <sup>-/-</sup> CT18 Rep B
128	<i>Bmal1</i> <sup>-/-</sup> CT18 Rep C
129	<i>Bmal1</i> <sup>-/-</sup> CT30 Rep A
130	<i>Bmal1</i> <sup>-/-</sup> CT30 Rep B
131	<i>Bmal1</i> <sup>-/-</sup> CT30 Rep C

### Proteomics: Clean-up and LC-MS/MS analysis

Peptides dried by vacuum centrifugation were cleaned up in preparation for LC-MS/MS analysis using C18 Stage Tips with a centrifuge-based protocol. Peptides were then aliquoted and taken to dryness by vacuum centrifugation and may be stored at  $-80^{\circ}\text{C}$  until required for LC-MS/MS analysis. Labelled peptide samples were resuspended in  $50\mu\text{l}$  0.1% TFA, sonicated for 15 minutes and injected ( $5\mu\text{l}$  per injection). Peptide mixtures were separated on a 50 cm,  $75\mu\text{m}$  I.D. Pepmap column over a 3 h gradient at  $40^{\circ}\text{C}$  and eluted directly into the mass spectrometer (Thermo Q Exactive Orbitrap). Xcalibur software was used to control the data acquisition. The instrument was run in data dependent acquisition mode with the top 10 most abundant peptides selected for tandem mass spectrometry (MS/MS) by higher energy collisional dissociation (HCD) fragmentation techniques. MS spectra were acquired at a resolution of 70,000 and an ion target of  $3 \times 10^6$ . HCD scans were performed with 35% normalised collision energy (NCE) at 35,000 resolution (at  $m/z$  200), and the ion target set to  $2 \times 10^5$  so as to avoid coalescence.

### Proteomics: Data analysis

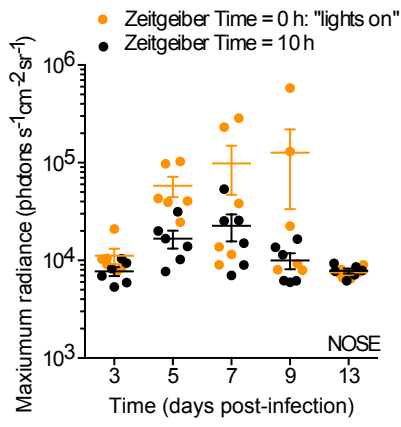
MaxQuant v1.5.2.8 was used to process the raw data acquired with a reporter ion quantification method. The Uniprot KB database of mouse sequences was used for peptide identification. Peptides identified with confidence interval (CI) values above 95% were used for protein identification and quantification. Database searching parameters included precursor ion mass tolerance of 5 ppm and fragment mass tolerance of 0.02 Da, digestion by trypsin, TMT 6-plex modification of peptide N-termini and lysine residues, with dynamic modifications at oxidation (M), deamination (N,Q), in addition to the static modifications at Methylthio (C). A peptide estimated false discovery rate (FDR) of 0.1% was used to generate tables with protein and peptide identifications and quantifications. Feature matching was enabled between runs for peptide identification. Reporter ion intensity (corrected and uncorrected) was imported into Perseus v1.5.2.6 for statistical analysis. Summary statistics were calculated on  $\log_2$  transformed reporter ion intensities. Data quality obtained from the TMT-based quantitative proteomics analysis was checked by S-curve analysis, and polygon and volcano plots. Corrected intensities were normalised by subtracting the mean value for each reporter ion column from each intensity within that column. Histograms revealed normal distributions centred on zero, confirming that this transformation was successful. To compare values more easily, data for each protein was normalised by the  $z$ -score method across all time-points and genotypes. These values were then used for subsequent analysis. Two-tailed  $t$ -tests were performed in Perseus using a false discovery rate (FDR) cut-off of 0.05 and a within groups variance  $S_0$  factor of 0.1. FDR was calculated by permutation-based method using  $n=250$  permutations per test. Proteins showing significant difference between CT18 and CT30 in WT cells, but not *Bmall*<sup>-/-</sup> cells, were subsequently tested via two-tailed  $t$ -test for significant differences between WT and *Bmall*<sup>-/-</sup> cells at both CT18 and CT30 (FDR cut-off 0.05) and presented graphically in R using the HeatMap

package (See Fig. S7). Proteins meeting both significance criteria were then subject to DAVID Functional Annotation Clustering analysis (See Table S1 and Table S2). Outputs were graphically presented using Cytoscape EnrichmentMap application and annotated using Clustermaker Markov Cluster Algorithm and WordCloud.

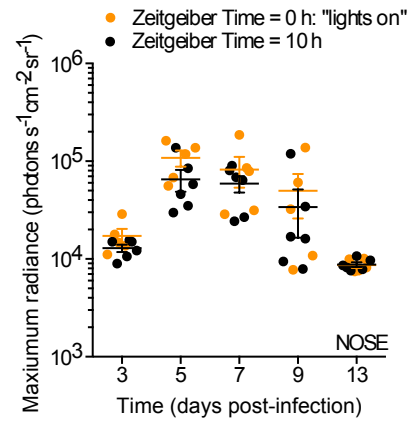
### Statistical analysis

For animal experiments, two-way analysis of variance (ANOVA) was performed on  $\text{Log}_{10}$ -transformed values. Normality and equality of variance were confirmed by the Kolmogorov-Smirnov test and Levene's median test respectively. Multiple two-tailed  $t$ -tests with FDR cut-off of 0.05 were also performed (\* $P$ <0.05, \*\* $P$ <0.01, \*\*\* $P$ <0.001). For cellular assays with multiple groups, ANOVA was performed with Holm-Sidak correction for multiple comparisons (\* $P$ <0.05, \*\* $P$ <0.01, \*\*\* $P$ <0.001). Equality of variance was confirmed via Brown-Forsythe test. For cellular assays with two groups, two-tailed  $t$ -tests with Welch's correction were performed.  $F$ -tests were used to compare variances and variances were not significantly different unless stated. For luciferase herpesvirus cellular assays, raw bioluminescence values were background-subtracted (bioluminescence – bioluminescence at  $t = 0$ h post-infection) and total bioluminescence calculated using the area under curve (AUC) method. For each experiment, total bioluminescence values were normalized (0% = bioluminescence at  $t = 0$ -1h; 100% = maximum total bioluminescence value). For analysis of virus replication kinetic parameters (Hill slope, time to 50% peak infection, and time to 50% decrease from peak infection), raw bioluminescence values were subject to asymmetric sigmoidal non-linear regression as illustrated in Fig. 3B, with goodness of fit reported by the coefficient of determination,  $R^2$ . Pearson's analysis was performed to test for correlations, with the correlation coefficient ( $r$ ) and two-tailed  $P$  values reported. PB2::GLUC IAV cellular assays, raw bioluminescence values were background-subtracted (PB2::LUC-infected bioluminescence – mock-infected bioluminescence). Values were subject to sigmoidal dose-response (variable slope) non-linear regression to determine plateau bioluminescence, with goodness of fit reported by  $R^2$ . Total IAV PB2::GLuc bioluminescence was calculated using the area under curve (AUC) method.

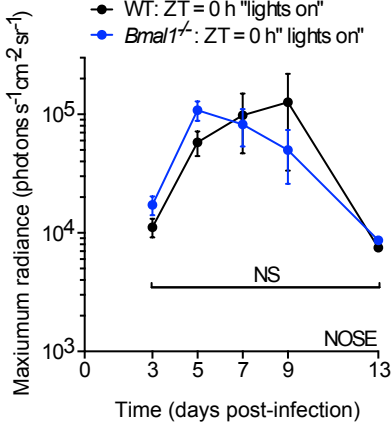
A



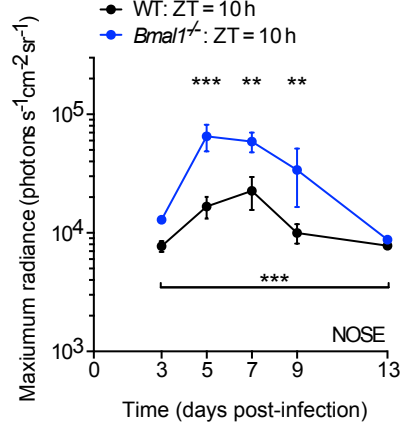
B



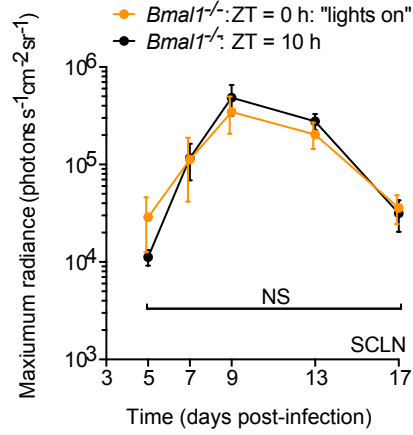
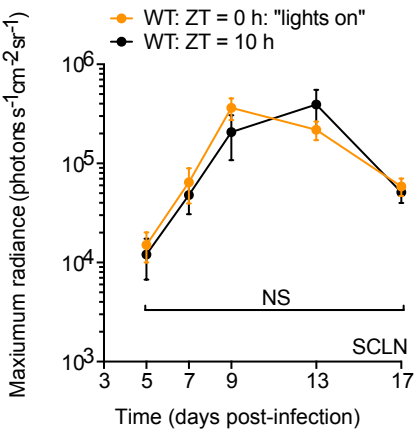
C



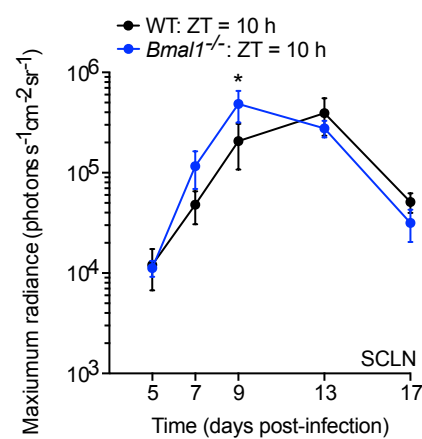
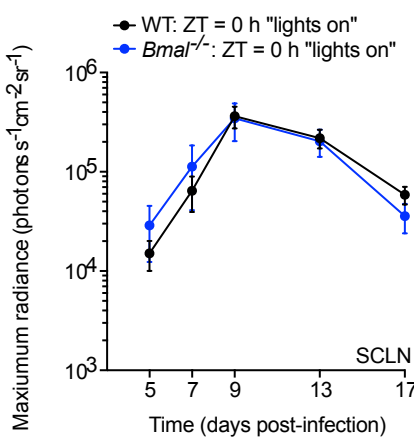
D

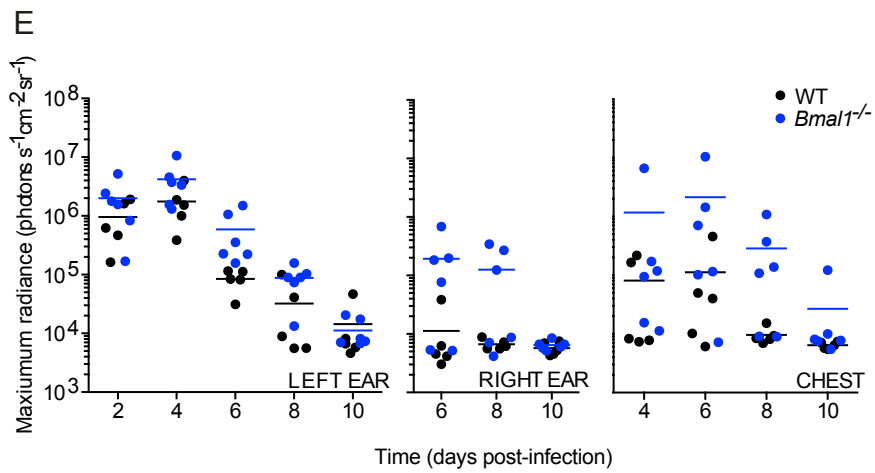
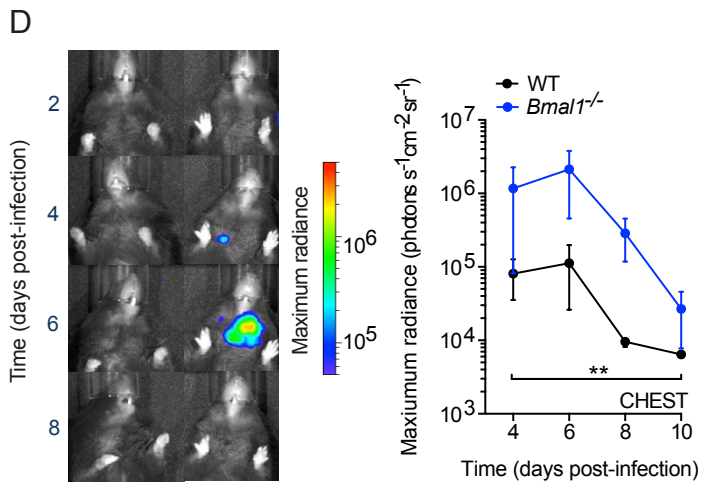
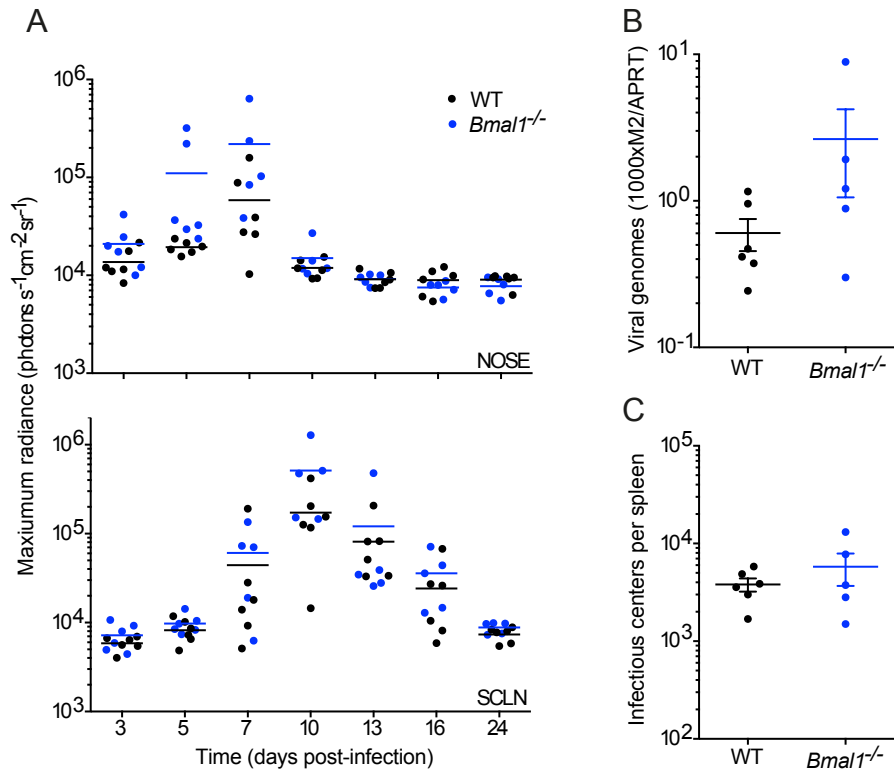


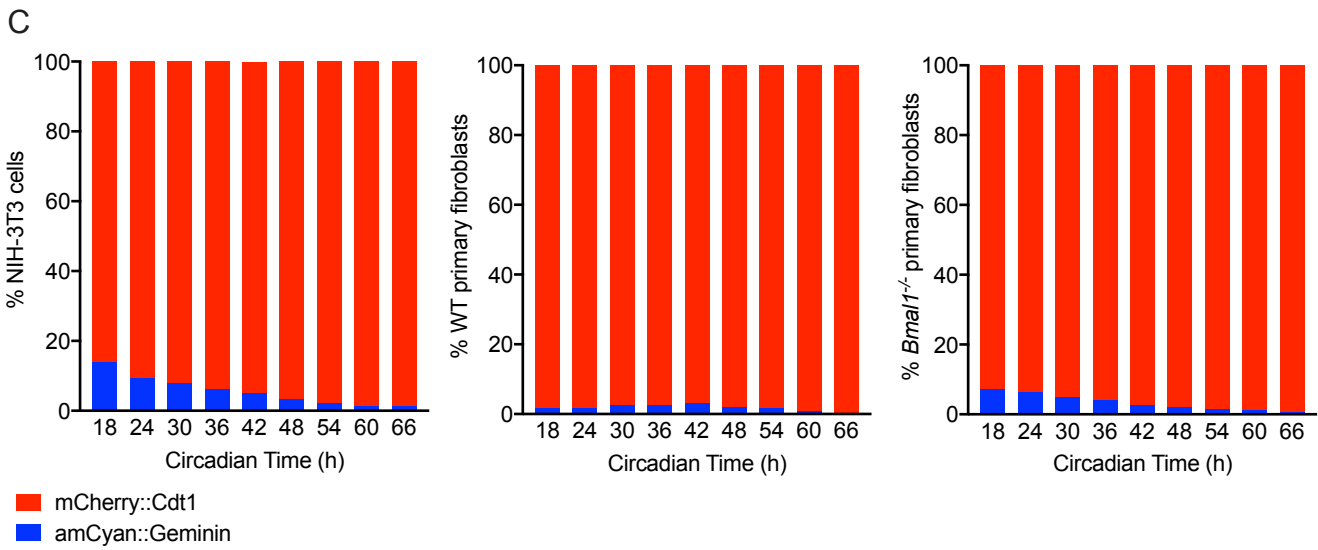
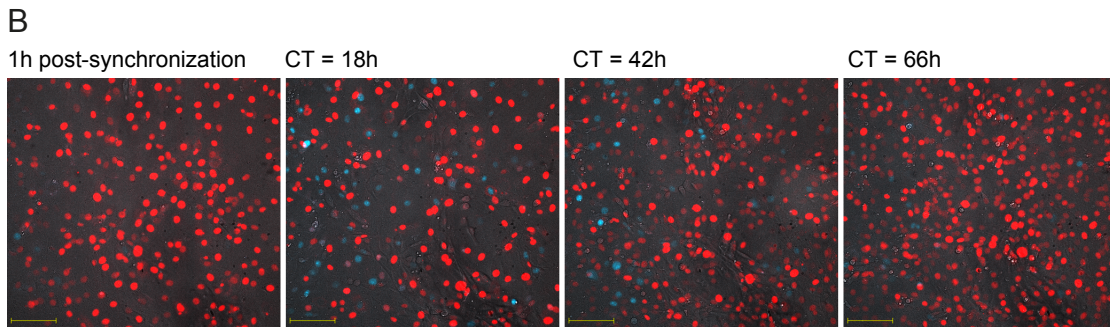
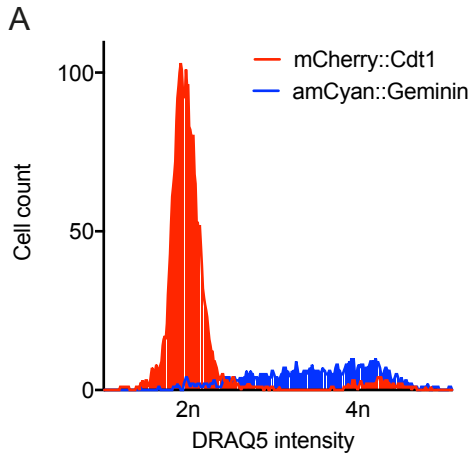
E



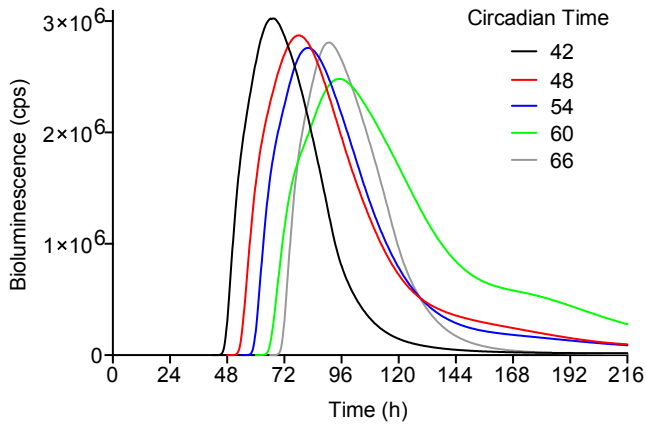
F







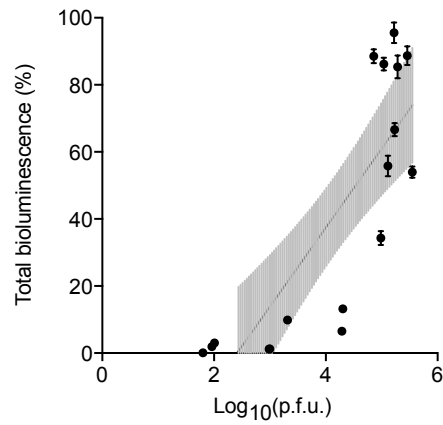
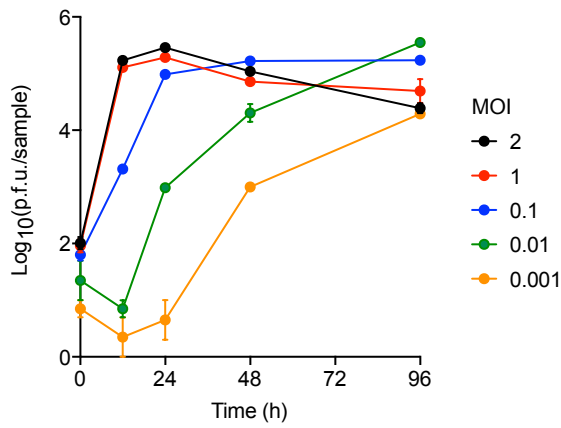
A



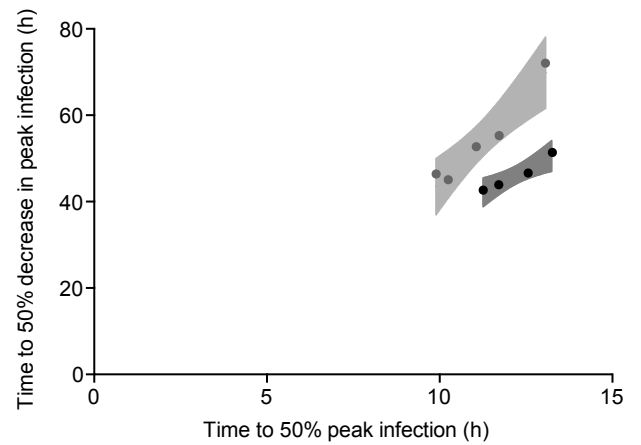
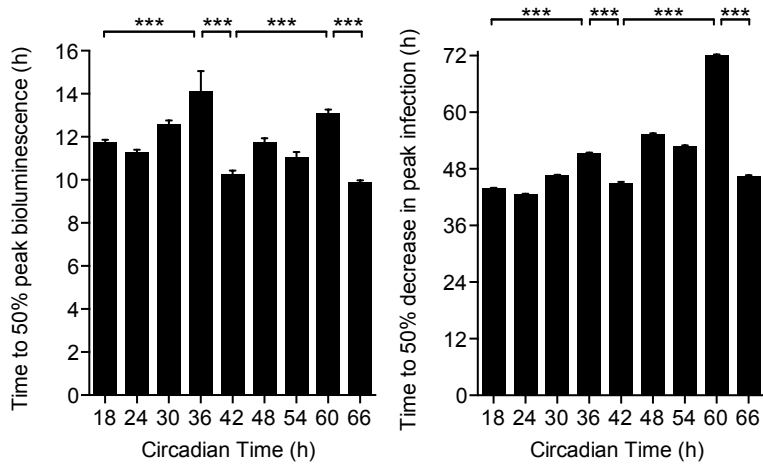
B

Circadian Time (h)	R <sup>2</sup> :Asymmetric sigmoidal curve fit UP	R <sup>2</sup> :Asymmetric sigmoidal curve fit DOWN
12	0.9674	0.9936
18	0.9724	0.9864
24	0.9403	0.9617
30	0.9948	0.8757
36	0.9247	0.9328
42	0.908	0.8997
48	0.917	0.8994
54	0.96	0.9781
60	0.9831	0.9708

C



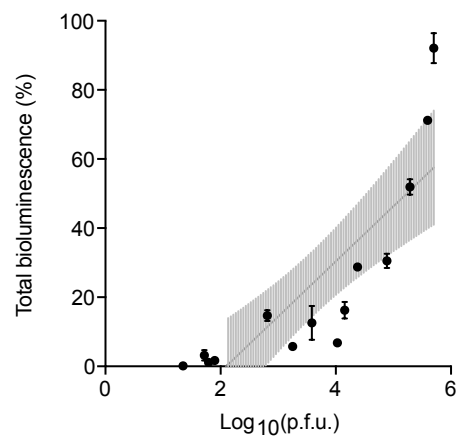
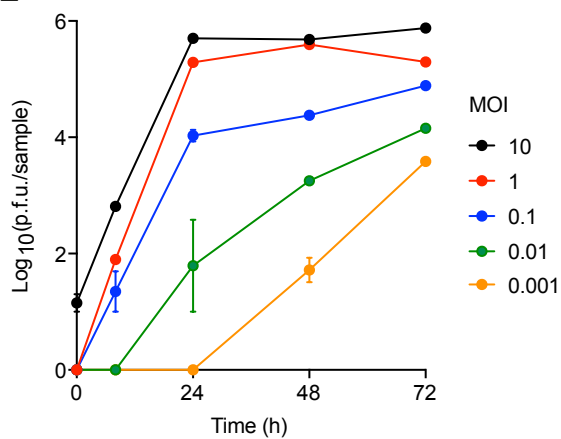
D

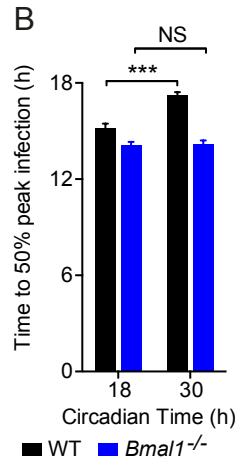
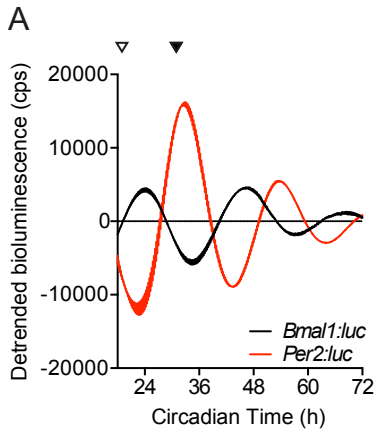


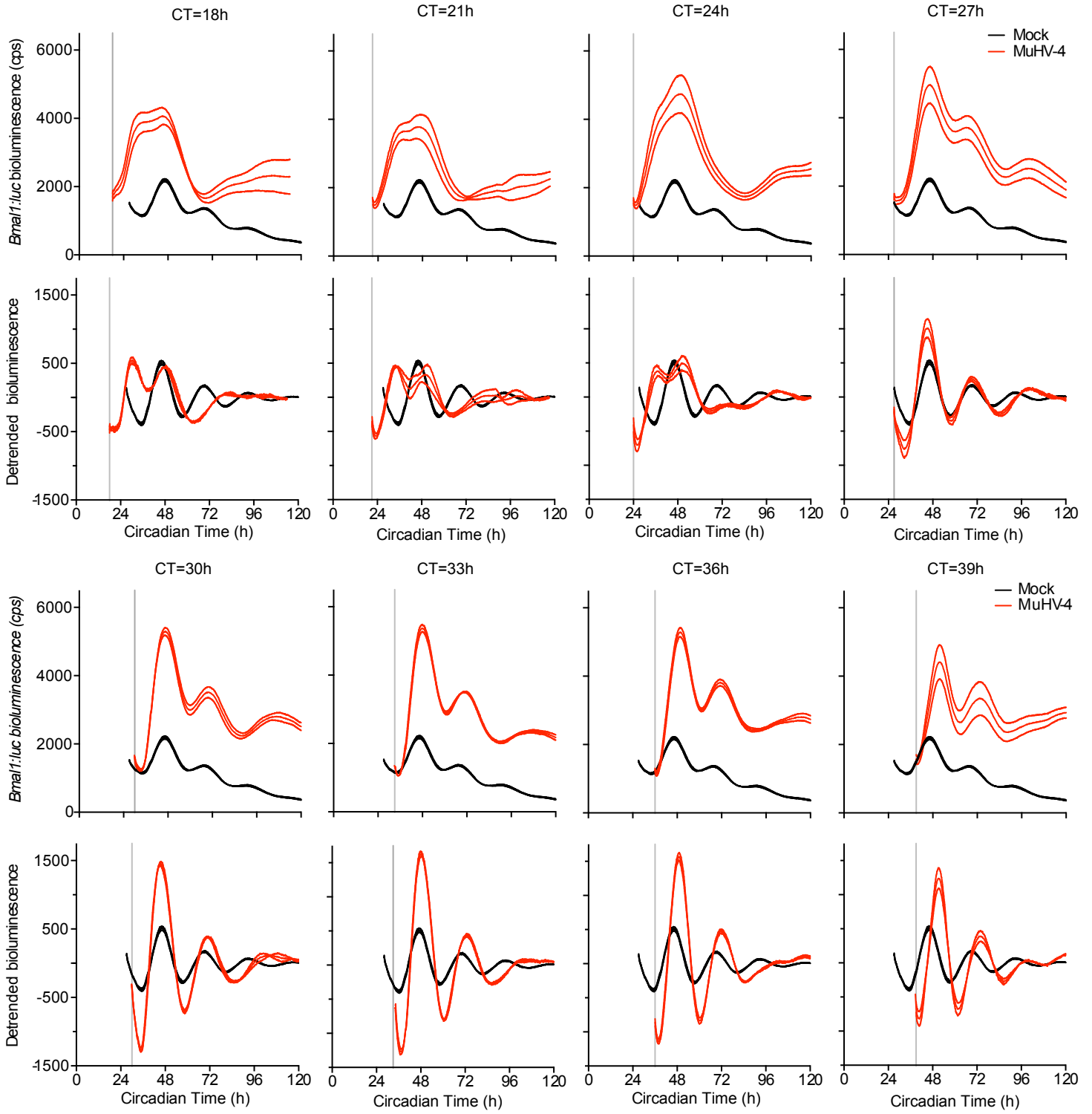
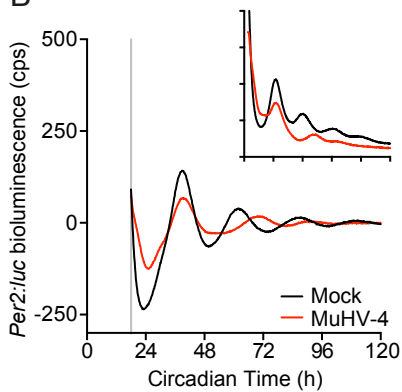
● Circadian Time 18 - 36h:  $P=0.022$

● Circadian Time 42 - 66h:  $P=0.006$

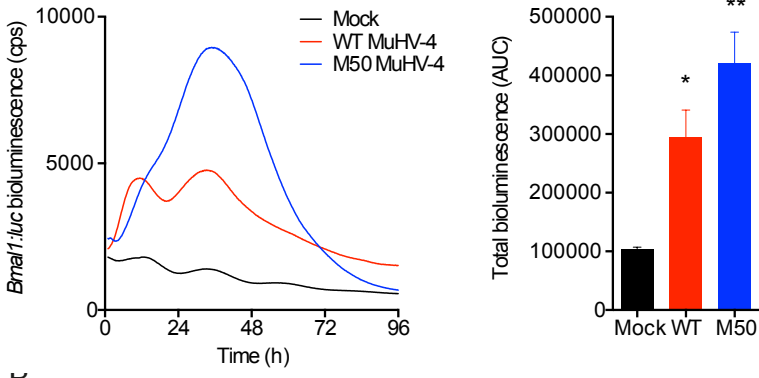
E



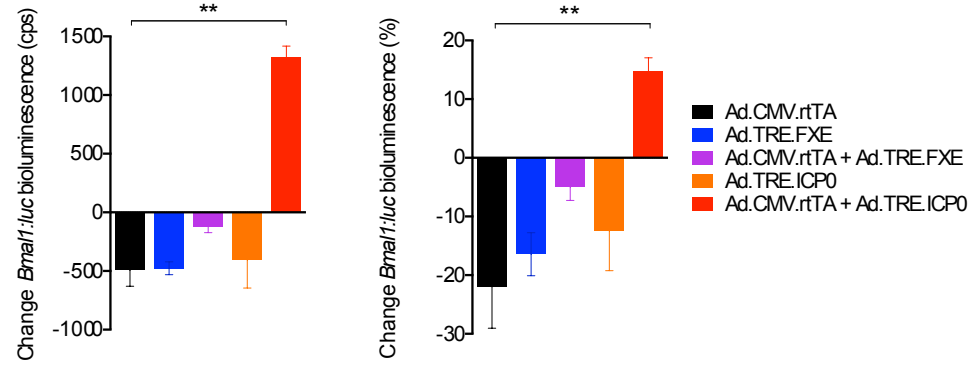
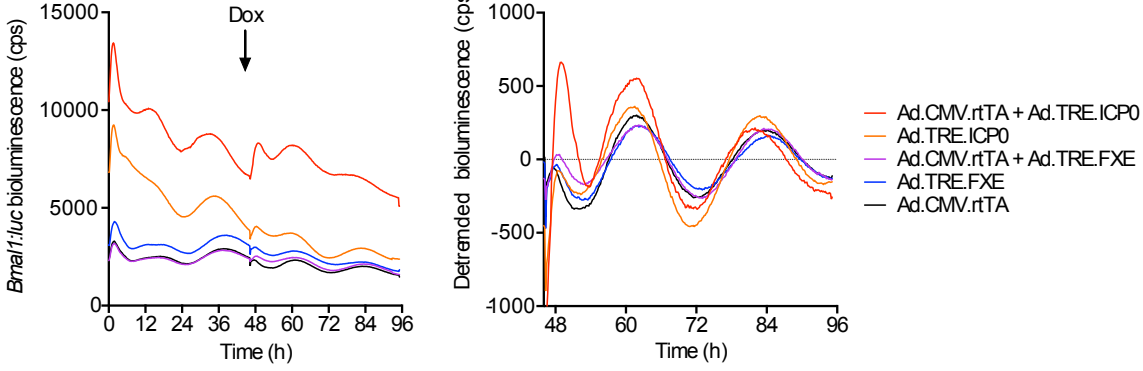


**A****B**

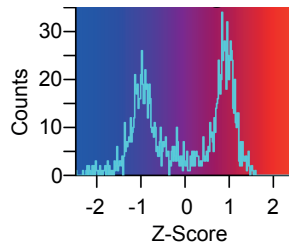
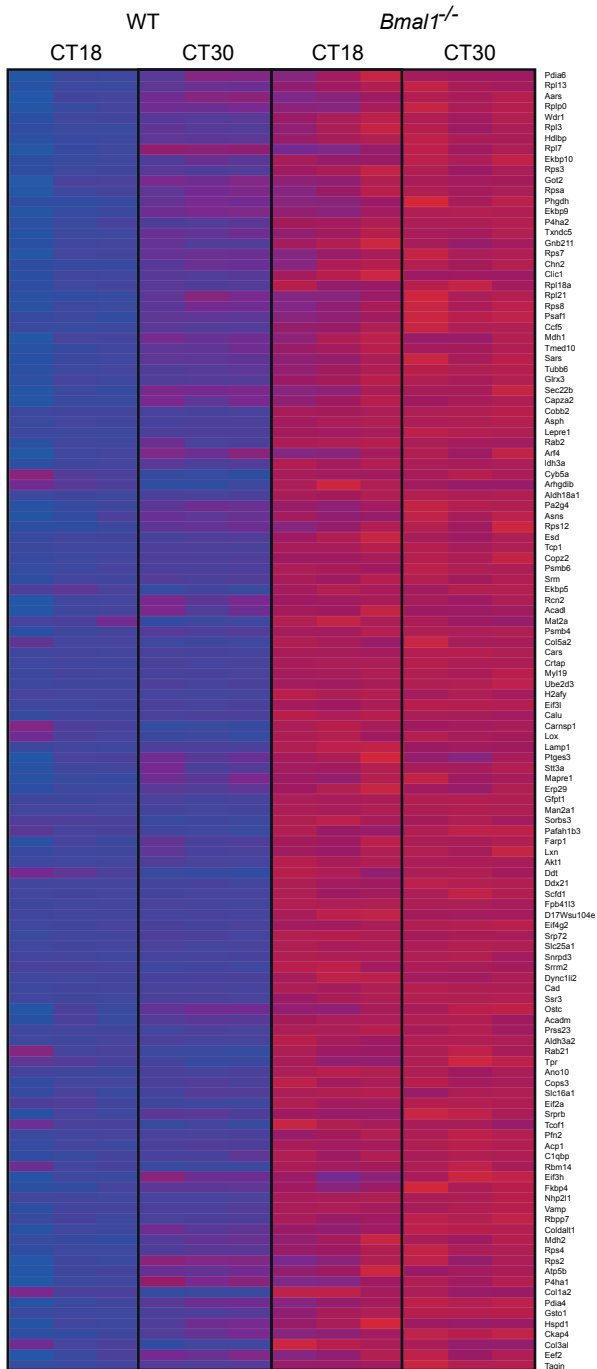
**A**



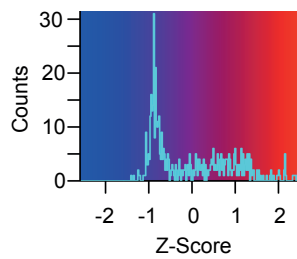
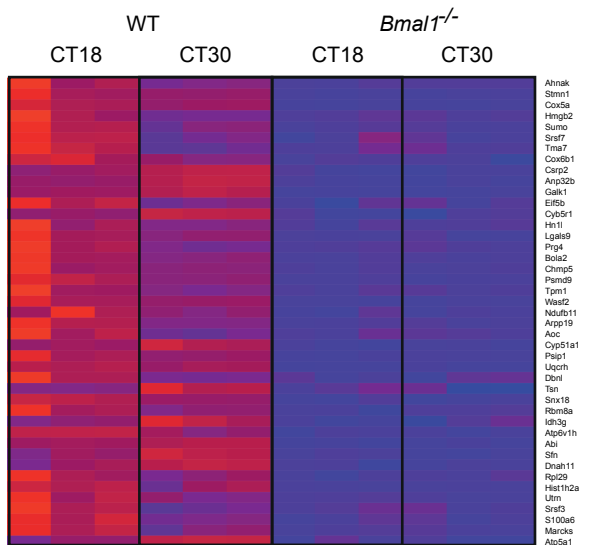
**B**



A



B



Gene Ontology Term	Gene IDs	Fold Enrichment	P =
<b>Enrichment Score: 7.333</b>			
Endoplasmic reticulum part	RAB2B, FKBP9, ERP29, PDIA6, PDIA4, CALU, STT3A, P4HA2, P4HA1, TXNDC5, SEC22B, ASPH, FKBP10, SSR3, RCN2	7.88	5.13E-09
Endoplasmic reticulum lumen	FKBP9, P4HA2, P4HA1, TXNDC5, ERP29, PDIA6, PDIA4, FKBP10, RCN2, CALU	16.86	6.22E-09
Endoplasmic reticulum	RAB2A, RAB2B, FKBP9, CKAP4, ERP29, PDIA6, PDIA4, SRPRB, ALDH3A2, CALU, SCFD1, STT3A, LEPRE1, P4HA2, P4HA1, TXNDC5, SEC22B, ASPH, FKBP10, RAB21, RCN2, SSR3	3.19	3.15E-06
<b>Enrichment Score: 7.235</b>			
Translation	RPSA, CARS, RPL13, SARS, GM8730, AARS, EIF2A, EEF2, RPS2, RPS4X, RPS8, RPS7, RPS3, GM10653, EIF4G2, RPL7, GM6576, RPL18A, EIF3H, RPLP0, RPL21, RPS12, RPL3, EIF3L, TPR	8.91	6.66E-15
Structural constituent of ribosome	RPSA, RPL13, GM8730, RPS2, RPS4X, RPS8, RPS3, RPS7, GM10653, GM6576, RPL18A, RPL7, RPL21, RPLP0, RPS12, RPL3	11.62	1.78E-10
Ribonucleoprotein complex	RPSA, RPL13, NHP2L1, SNRPD3, GM8730, EEF2, SRPRB, RPS2, RPS4X, RPS8, RPS7, RPS3, GM10653, PA2G4, RPL7, GM6576, RPL18A, RPLP0, SRRM2, RPL21, RPS12, RPL3, SRP72	5.52	7.52E-10
Ribosome	RPSA, RPL13, GM8730, RPS2, RPS4X, RPS8, RPS3, RPS7, GM10653, GM6576, RPL18A, RPL7, RPL21, RPLP0, RPS12, RPL3	8.85	4.97E-09
Structural molecule activity	RPSA, RPL13, GM8730, COL3A1, RPS2, RPS4X, COL5A2, RPS8, RPS7, RPS3, GM10653, COPB2, RPL7, GM6576, RPL18A, RPL21, RPLP0, RPS12, COL1A2, RPL3, TUBB6	5.29	1.30E-08
Small ribosomal subunit	GM10653, RPSA, GM6576, RPS4X, RPS2, RPS3	20.93	8.47E-05
Non-membrane-bounded organelle	DYNC1LI2, RPL13, NHP2L1, CAPZA2, TCOF1, RPS2, RPS3, MYL9, GM10653, AKT1, PFN2, SORBS3, RPL7, GM6576, RPLP0, RPL3, EIF3L, H2AFY, TUBB6, DDX21, RPSA, TCP1, GM8730, RPS4X, RPS8, FARP1, RPS7, PA2G4, RPL18A, RPL21, RPS12, SRP72, WDR1, MAPRE1	2.02	8.96E-05
Ribosomal subunit	GM10653, RPSA, RPL7, GM6576, RPS4X, RPS2, RPS3	11.04	1.97E-04
<b>Enrichment Score: 5.729</b>			
Endoplasmic reticulum lumen	FKBP9, P4HA2, P4HA1, TXNDC5, ERP29, PDIA6, PDIA4, FKBP10, RCN2, CALU	16.86	6.22E-09
Intracellular organelle lumen	FKBP9, NHP2L1, TCOF1, PDIA6, PDIA4, CALU, GOT2, P4HA2, P4HA1, SRRM2, EIF3L, DDX21, ACADM, ERP29, ACADL, RBBP7, PA2G4, C1QBP, TXNDC5, SRP72, HSPD1, RBM14, FKBP10, MDH2, RCN2	2.68	1.01E-05
<b>Enrichment Score: 3.707</b>			
Glutamine family amino acid metabolic process	GOT2, ALDH18A1, GFPT1, PHGDH, ASNS, CAD	17.24	2.29E-05
Amine biosynthetic process	GOT2, ALDH18A1, MAT2A, SRM, PHGDH, ASNS, PSAT1	11.85	2.55E-05
Cellular amino acid biosynthetic process	GOT2, ALDH18A1, MAT2A, PHGDH, ASNS, PSAT1	16.84	2.56E-05
Carboxylic acid biosynthetic process	GOT2, PTGES3, ALDH18A1, MAT2A, PHGDH, ASNS, GSTO1, PSAT1	7.01	1.38E-04
Nitrogen compound biosynthetic process	GOT2, ALDH18A1, MAT2A, SRM, ATP5B, PHGDH, ASNS, CAD, PSAT1	3.68	2.96E-03
Aspartate family amino acid metabolic process	GOT2, PHGDH, ASNS	16.84	1.33E-02
<b>Enrichment Score: 3.484</b>			
Pigment granule	RAB2A, LAMP1, ERP29, TMED10, SEC22B, PDIA6, PDIA4, CALU	11.43	5.73E-06
Melanosome	RAB2A, LAMP1, ERP29, TMED10, SEC22B, PDIA6, PDIA4, CALU	11.43	5.73E-06
Cytoplasmic membrane-bounded vesicle	RAB2A, COPZ2, CAPZA2, ERP29, ESD, PDIA6, PDIA4, CALU, COPB2, LAMP1, TMED10, SEC22B, VAMP2, HSPD1, RAB21	4.40	6.37E-06
Cytoplasmic vesicle	RAB2A, COPZ2, CAPZA2, ERP29, ESD, PDIA6, PDIA4, CALU, COPB2, LAMP1, TMED10, SEC22B, VAMP3, VAMP2, HSPD1, RAB21	3.82	1.48E-05
Endomembrane system	COPZ2, RAB2B, CAPZA2, CLIC1, MAN2A1, COPB2, STT3A, TMED10, SEC22B, VAMP2, ASPH, TPR, RAB21, SSR3	3.18	3.97E-04

Cytoplasmic vesicle membrane	COPZ2, COPB2, CAPZA2, TMED10, VAMP2, RAB21	8.37	7.12E-04
Golgi apparatus part	COPZ2, COPB2, RAB2B, MAN2A1, TMED10, SEC22B, VAMP2, RAB21	4.28	2.54E-03
Golgi apparatus	COPZ2, RAB2A, COPB2, RAB2B, MAN2A1, SCFD1, ARF4, TMED10, SEC22B, VAMP2, MAPRE1, RAB21	2.14	2.30E-02
<b>Enrichment Score: 3.081</b>			
Protein folding	FKBP9, CCT5, TCP1, FKBP5, FKBP4, AARS, HSPD1, FKBP10	7.78	7.14E-05
Peptidyl-prolyl cis-trans isomerase activity	FKBP9, FKBP5, FKBP4, FKBP10	14.33	2.61E-03
<b>Enrichment Score: 2.076</b>			
Endomembrane system	COPZ2, RAB2B, CAPZA2, CLIC1, MAN2A1, COPB2, STT3A, TMED10, SEC22B, VAMP2, ASPH, TPR, RAB21, SSR3	3.18	3.97E-04
Nuclear envelope-ER network	RAB2B, STT3A, SEC22B, ASPH, SSR3	3.79	4.18E-02
<b>Enrichment Score: 1.969</b>			
Procollagen-proline dioxygenase activity	LEPRE1, P4HA2, P4HA1	53.73	1.27E-03
Peptidyl-proline dioxygenase activity	LEPRE1, P4HA2, P4HA1	53.73	1.27E-03
Oxidoreductase activity (paired donors)	LEPRE1, P4HA2, P4HA1, ASPH	16.71	1.67E-03
L-ascorbic acid binding	LEPRE1, P4HA2, P4HA1	18.80	1.07E-02
Vitamin binding	GOT2, LEPRE1, P4HA2, P4HA1, PSAT1	5.18	1.55E-02
Carboxylic acid binding	LEPRE1, P4HA2, P4HA1, CAD	5.90	2.97E-02
<b>Enrichment Score: 1.946</b>			
tRNA aminoacylation for protein translation	CARS, SARS, AARS, TPR	10.74	5.93E-03
tRNA aminoacylation	CARS, SARS, AARS, TPR	10.74	5.93E-03
Amino acid activation	CARS, SARS, AARS, TPR	10.74	5.93E-03
Ligase activity (aminoacyl-tRNA)	CARS, SARS, AARS, TPR	10.45	6.41E-03
<b>Enrichment Score: 1.903</b>			
Endomembrane system	COPZ2, RAB2B, CAPZA2, CLIC1, MAN2A1, COPB2, STT3A, TMED10, SEC22B, VAMP2, ASPH, TPR, RAB21, SSR3	3.18	3.97E-04
Golgi apparatus part	COPZ2, COPB2, RAB2B, MAN2A1, TMED10, SEC22B, VAMP2, RAB21	4.28	2.54E-03
Golgi membrane	COPZ2, COPB2, RAB2B, MAN2A1, SEC22B, RAB21	5.32	5.23E-03
Protein transport	RAB2A, COPZ2, RAB2B, ERP29, COPB2, SCFD1, ARF4, TMED10, SEC22B, SRP72, TPR, RAB21, SSR3	2.47	5.91E-03
Protein localization	RAB2A, COPZ2, RAB2B, ERP29, COPB2, SCFD1, ARF4, TMED10, SEC22B, SRP72, TPR, GNB2L1, RAB21, SSR3	2.30	7.19E-03
Vesicle-mediated transport	COPZ2, RAB2A, COPB2, RAB2B, SCFD1, ARF4, TMED10, SEC22B, VAMP3, VAMP2	2.65	1.26E-02
Golgi apparatus	COPZ2, RAB2A, COPB2, RAB2B, MAN2A1, SCFD1, ARF4, TMED10, SEC22B, VAMP2, MAPRE1, RAB21	2.14	2.30E-02
Intracellular protein transport	COPZ2, RAB2A, COPB2, TMED10, SRP72, TPR, SSR3	3.13	2.37E-02
<b>Enrichment Score: 1.597</b>			
Cofactor binding	GOT2, ACADM, PHGDH, ACADL, PSAT1, IDH3A, MDH1	3.88	9.02E-03
Coenzyme binding	ACADM, PHGDH, ACADL, IDH3A, MDH1	3.92	3.80E-02
NAD or NADH binding	PHGDH, IDH3A, MDH1	8.55	4.72E-02
<b>Enrichment Score: 1.596</b>			
Nucleotide binding	DYNC1LI2, ALDH18A1, ATP5B, FKBP4, ASNS, CAD, AKT1, UBE2D3, TUBB6, DDX21, TPR, RAB21, RAB2A, RAB2B, CARS, TCP1, ACADM, MAT2A, SARS, AARS, EEF2, SRPRB, ACADL, IDH3A, CCT5, ARF4, PHGDH, HSPD1, RBM14, MDH1	1.72	2.56E-03
Purine nucleotide binding	DYNC1LI2, ALDH18A1, ATP5B, FKBP4, ASNS, CAD, AKT1, UBE2D3, TUBB6, DDX21, TPR, RAB21, RAB2A, RAB2B, CARS, TCP1, ACADM, MAT2A, SARS, AARS, EEF2, SRPRB, ACADL, CCT5, ARF4, HSPD1	1.74	5.06E-03

Ribonucleotide binding	RAB2A, RAB2B, TCP1, CARS, DYNC1LI2, ALDH18A1, MAT2A, SARS, ATP5B, FKBP4, AARS, ASNS, CAD, EEF2, SRPRB, AKT1, UBE2D3, CCT5, ARF4, TUBB6, DDX21, HSPD1, TPR, RAB21	1.68	1.20E-02
<b>Enrichment Score: 1.591</b>			
Organelle membrane	COPZ2, RAB2B, ALDH18A1, ATP5B, CAPZA2, ALDH3A2, GOT2, COPB2, MAN2A1, STT3A, TMED10, SEC22B, SLC25A1, VAMP2, HSPD1, ASPH, RAB21, MDH2, SSR3	2.85	8.52E-05
Mitochondrial matrix	GOT2, ACADM, C1QBP, HSPD1, ACADL, MDH2	4.47	1.07E-02
Mitochondrial part	GOT2, ACADM, ALDH18A1, C1QBP, ATP5B, SLC25A1, HSPD1, ACADL, ALDH3A2, MDH2	2.32	2.71E-02
Mitochondrial inner membrane	GOT2, ALDH18A1, ATP5B, SLC25A1, HSPD1, ALDH3A2, MDH2	2.87	3.40E-02
<b>Enrichment Score: 1.458</b>			
Collagen	COL3A1, COL1A2, LOX, COL5A2	25.56	4.64E-04
Collagen fibril organization	P4HA1, COL3A1, LOX, COL5A2	23.53	6.01E-04
SMAD binding	COL3A1, COL1A2, COL5A2	18.80	1.07E-02
Extracellular matrix structural constituent	COL3A1, COL1A2, COL5A2	12.54	2.33E-02
<b>Enrichment Score: 1.404</b>			
Energy derivation by oxidation	PTGES3, AKT1, IDH3A, MDH2, MDH1	6.30	7.95E-03
Tricarboxylic acid cycle	IDH3A, MDH2, MDH1	16.11	1.45E-02
Acetyl-CoA catabolic process	IDH3A, MDH2, MDH1	15.44	1.57E-02
Aerobic respiration	IDH3A, MDH2, MDH1	13.73	1.96E-02
Coenzyme catabolic process	IDH3A, MDH2, MDH1	12.78	2.25E-02
Acetyl-CoA metabolic process	IDH3A, MDH2, MDH1	11.95	2.55E-02
Cofactor catabolic process	IDH3A, MDH2, MDH1	11.58	2.70E-02
<b>Enrichment Score: 1.363</b>			
Energy derivation	PTGES3, AKT1, IDH3A, MDH2, MDH1	6.30	7.95E-03
Hexose metabolic process	PTGES3, AKT1, MAN2A1, MDH2, MDH1	3.65	4.70E-02
<b>Enrichment Score: 1.332</b>			
Vesicle-mediated transport	COPZ2, RAB2A, COPB2, RAB2B, SCFD1, ARF4, TMED10, SEC22B, VAMP3, VAMP2	2.65	1.26E-02
Exocytosis	SCFD1, TMED10, VAMP3, VAMP2	4.49	5.85E-02
<b>Enrichment Score: 1.109</b>			
GTP binding	RAB2A, RAB2B, FKBP4, ARF4, TUBB6, EEF2, SRPRB, RAB21	2.83	2.21E-02
guanyl nucleotide binding	RAB2A, RAB2B, FKBP4, ARF4, TUBB6, EEF2, SRPRB, RAB21	2.76	2.49E-02
guanyl ribonucleotide binding	RAB2A, RAB2B, FKBP4, ARF4, TUBB6, EEF2, SRPRB, RAB21	2.76	2.49E-02
<b>Enrichment Score: 0.089</b>			
Regulation of translation	AKT1, EIF4G2, PA2G4, EIF2A	4.94	4.64E-02

Gene Ontology Term	Gene IDs	Fold Enrichment	P =
<b>Enrichment Score: 2.235</b>			
Hydrogen ion transmembrane transporter activity	UQCRH, COX6B1, ATP6V1H, ATP5A1, COX5A	22.51	6.10E-05
Generation of precursor metabolites and energy	NDUFB11, IDH3G, UQCRH, ATP6V1H, ATP5A1	7.44	3.92E-03
Mitochondrial inner membrane	NDUFB11, UQCRH, COX6B1, ATP5A1, COX5A	6.81	5.19E-03
Oxidative phosphorylation	UQCRH, ATP6V1H, ATP5A1	20.80	8.60E-03
Mitochondrial membrane	NDUFB11, UQCRH, COX6B1, ATP5A1, COX5A	5.48	1.10E-02
Mitochondrial envelope	NDUFB11, UQCRH, COX6B1, ATP5A1, COX5A	5.16	1.36E-02
Organelle membrane	NDUFB11, UQCRH, COX6B1, ATP6V1H, ATP5A1, COX5A	2.99	4.15E-02
<b>Enrichment Score: 2.219</b>			
Nucleosome	HIST1H2AB, HIST1H2AA, HIST1H2AF, HIST1H2AD, HIST1H2AH, HIST3H2A	26.02	4.28E-04
Protein-DNA complex	HIST1H2AB, HIST1H2AA, HIST1H2AF, HIST1H2AD, HIST1H2AH, HIST3H2A	21.51	7.49E-04
Nucleosome assembly	HIST1H2AB, HIST1H2AA, HIST1H2AF, HIST1H2AD, HIST1H2AH, HIST3H2A	21.27	7.90E-04
Chromatin assembly	HIST1H2AB, HIST1H2AA, HIST1H2AF, HIST1H2AD, HIST1H2AH, HIST3H2A	20.71	8.55E-04
DNA packaging	HIST1H2AB, HIST1H2AA, HIST1H2AF, HIST1H2AD, HIST1H2AH, HIST3H2A	15.38	2.02E-03
Cellular macromolecular complex subunit organization	HIST1H2AB, HIST1H2AA, HIST1H2AF, HIST1H2AD, HIST1H2AH, HIST3H2A, STMN1	7.92	3.13E-03
Chromosome	HIST1H2AB, HMGB2, HIST1H2AA, HIST1H2AF, HIST1H2AD, HIST1H2AH, HIST3H2A	5.34	1.21E-02
<b>Enrichment Score: 2.012</b>			
Lamellipodium	DBNL, WASF2, ABI2, ABI1	25.61	4.49E-04
Cell leading edge	DBNL, WASF2, ABI2, ABI1	14.41	2.38E-03
Cytoskeleton	DBNL, UTRN, WASF2, ABI2, ABI1, MARCKS, STMN1, TPM1	2.88	1.49E-02
Cell projection	DBNL, UTRN, WASF2, ABI2, ABI1	3.51	4.70E-02
<b>Enrichment Score: 1.834</b>			
Non-membrane-bounded organelle	HIST1H2AB, DBNL, HMGB2, HIST1H2AA, HIST1H2AF, HIST1H2AD, WASF2, UTRN, ABI2, GM5218, ABI1, TPM1, RPL29, HIST1H2AH, GM10709, MARCKS, HIST3H2A, STMN1	2.94	2.30E-04
Cytoskeletal protein binding	DBNL, UTRN, WASF2, MARCKS, STMN1, TPM1	5.35	4.30E-03
Actin binding	DBNL, UTRN, WASF2, MARCKS, TPM1	6.41	6.67E-03
Cytoskeleton	DBNL, UTRN, WASF2, ABI2, ABI1, MARCKS, STMN1, TPM1	2.88	1.49E-02
Cell cortex	DBNL, UTRN, MARCKS	9.60	3.65E-02
<b>Enrichment Score: 1.494</b>			
Oxidative phosphorylation	UQCRH, ATP6V1H, ATP5A1	20.80	8.60E-03
Phosphorylation	GALK1, UQCRH, ABI2, ATP6V1H, ABI1, ATP5A1	3.24	3.17E-02
<b>Enrichment Score: 0.536</b>			
Oxidation reduction	CYB5R1, NDUFB11, IDH3G, UQCRH, AOC2, AOC3	3.47	2.47E-02